Stability Analysis of the Ancient Sevier Gravity Slide, Southwest Marysvale Volcanic Field, Utah

Undergraduate Research Thesis

Submitted in partial fulfillment of the requirements for graduation

with research distinction in Earth Science

In the undergraduate colleges of

The Ohio State University

By

Samuel Isaac Schneider

The Ohio State University

2020

Approved by

W. Ashley Griffith, Advisor
School of Earth Sciences

TABLE OF CONTENTS

ABSTRACT

The Sevier Gravity Slide (SGS) is a long-runout landslide, part of the Markagunt Gravity Slide Complex in the Marysvale Volcanic Field, southwest Utah. The SGS was a single catastrophic emplacement event, hypothesized to have initiated by failure of the volcanic field via gravitational stress perturbations. While initiation is agreed to be gravity driven, the regional stress state and the topography at the time of emplacement is unclear, as well as any potential triggering mechanisms. In this project, without considering triggering events, I vary far field stresses as well as the topographic surface to analyze their impacts on the subsurface stress distribution and potential for slide initiation. In the model, I idealize the problem as a single body, with an upper boundary acting as the paleo-topographic surface. The parameters of the model are the mechanical properties of the idealized rock body, the far field, tectonically driven stress field, the topographic surface and boundary conditions for that surface. I constrain the topographic surface as a free surface, maintaining zero shear and normal strength. Using the Boundary Element Method, I calculate topographically driven stress perturbations beneath the topography and superimpose those on the regional state of stress to create a full stress distribution beneath topography. Secondly, I place observation points along a potential detachment surface for the slide to calculate normal and shear stresses. With various far field stress states and topography, I analyze the effect on the shear stress along the potential detachment surface and infer which paleo-conditions are most preferential for potential detachment and initiation of the slide. The results of this model are taken to be a starting point in modeling the true initiation of the gravity slide, and potential initiation mechanism and their addition to the provided modeling framework is discussed.

ACKNOWLEDGEMENTS

My first thank you goes to my advisor Dr. Ashley Griffith for his guidance through this thesis process and more broadly for being an amazing mentor, teacher, and friend. Also, a huge thank you to our lab group members, specifically Caje Kindred, Michael Braunagel, and Zachary Smith. I couldn't have done this project without Ashley and the rest of this team embracing me and giving me constant support. I immensely appreciate my time spent within this research group.

Thank you to my family and my friends for your support throughout my life and especially through my development in college. Thank you to my parents, Mitchell and Kyla Schneider, and my siblings Keeva, Ramie, and Sari for your unconditional love. Thank you to my friends for being the truest of gentlemen.

I'd like to give a special thank you to the School of Earth Sciences community including the students, faculty, staff, and alumni. Our close-knit community is a unique place I've found at Ohio State and I will miss all of the daily engagements within Mendenhall. Thank you to the great friends I've made in my time here at SES, especially our Field Camp 2019 cohort. That summer will always be a favorite of mine. Thank you to our donors, as the recipient of scholarships from the School of Earth Sciences Field Camp Experience Travel Fund and the William J. Buschman Scholarship Award, I've personally benefitted greatly from the generosity and support of our alumni. A special thanks to Dr. Anne Carey for her role as a guide through writing this thesis. Thank you to Dr. Derek Sawyer for being on my thesis committee. And thank you to all the other faculty for your continual commitment to the students at SES. I will surely miss our community!

LIST OF FIGURES

LIST OF TABLES

INTRODUCTION

Motivation and Goals

The volcanic sector collapse and subsequent Sevier Gravity Slide (SGS) in Southwest Utah is of extreme interest and is being studied collaboratively among researchers Dr. Ashley Griffith (The Ohio State University), Dr. David Hacker (Kent State University), and Dr. Robert Biek (Utah Geological Survey) and their students, as well as their collaborators Pete Rowley, Dr. Tiffany Rivera (Westminster University, Salt Lake City, Utah), and Dr. David Malone (Illinois State University), among others. The SGS is the oldest of three adjacent gravity slides, the others being the Markagunt and Black Hills Gravity Slides, shown in Figure 1, that resulted from sector collapse of the southern portion of the Marysvale Volcanic Field (e.g., Biek et al., 2019). Chief concern of the study is to constrain the timing and conditions leading to initiation and the mechanisms that lead to the mobility of the SGS, a slide unique among terrestrial counterparts for its long runout length. This collaborative project relies on mapping previously done by Biek and others and seeks investigation into the mechanical properties of rocks in the area, the structure of the basal sliding surface and paleo-topography, initiation mechanisms, and the influence of fluid pressure while sliding. All of this work requires an understanding of the paleo-environment and the subsurface state of stress at the time of sector collapse. As a part of this larger collaborative project, the work done in this thesis begins the process of modeling the initiation of the slide by exploring the stress conditions in the paleo-environment preceding slide initiation.

In this project, I develop a Boundary Element Method model using the Displacement Discontinuity Method to analyze slope stability of pre-slide conditions, based on geometrical constraints we currently have from geological mapping of the SGS in Southwest Utah. As a deep-seated gravity slide, the SGS is interpreted to have initiated due to gravitational perturbations in the stress field beneath topography and the related tractions resolved on a weak detachment surface. The model is developed to calculate stress distributions beneath a paleo-topographic surface to represent a cross-section of pre-slide conditions of the SGS. Stress distributions are calculated using Boundary Element Methods and are superimposed onto pre-defined far field stresses. Stress distributions are then compared to two failure criteria to assess slope stability.

Geologic Setting

The Marysvale Volcanic Field is one of the major volcanic fields in the southwestern United States, covering areas of both the Colorado Plateau and the Basin and Range Province. Most volcanic activity in Marysvale took place circa 32-14 Ma, and rocks are comprised more than 90% by volume of volcanic mudflow breccias or lava flows and less than 10% of ash-flow tuff (Steven et al., 1984; Rowley et al., 1994; Cunningham et al., 2007). The volcanism in Marysvale evolved from andesitic and calc-alkaline volcanism and intrusions into bimodal volcanism, producing rhyolite and basalts. At the time of deposition in the Oligocene, the field was dominated by clustered stratovolcanoes producing two intertonguing massive units of mudflow breccia, the Bullion Canyon and Mt. Dutton

Formations (Figure 2). Most of the rocks exposed in the southern part of the volcanic field belong to the Mt. Dutton Formation. (Biek et al., 2019).

Discovered and mapped only recently (Hacker et al., 2014; Biek et al., 2015; Biek et al., 2019) the Markagunt Gravity Slide Complex is a defining structural feature of the Marysvale area in Utah. Among the largest known terrestrial landslides ever, the slide complex consists of 3 individual landslides, younging from east to west, all sliding north, from the center of the volcanic pile, southward. The Markagunt Gravity Slide was discovered first (Hacker et al., 2014) and is younger than the subsequently discovered Sevier slide to the east (Biek et al., 2019). Subsequently, what was initially mapped as the Markagunt Gravity Slide was subdivided into the Black Mountains Gravity slide to the west and the Markagunt Gravity Slide to the east based on differing locations of the ramp fault (Biek et al., 2019). Field evidence collected in the mapping of these slides suggests that these slides were, respectively, catastrophic, single emplacement events representing sector collapse of the Marysvale volcanic zone, simultaneous with late stages of the volcanic field. (Hacker et al., 2014; Biek et al., 2019).

In the slide area, there exists a widespread uniformity of kinematic indicators such as slickenlines, grooves, and Reidel shears that indicate southward movement of the slide mass (Hacker et al., 2014). Source areas are therefore interpreted to be the Mt. Belknap and Monroe Peak Calderas for the Markagunt and Sevier Gravity Slides, respectively (top of Figure 1). These calderas represent high points of elevation within the Marysvale Volcanic Field explaining the southward movement of the mass away from the center of the field and toward the southern flat topography.

Mapping data collected from the Markagunt Gravity Slide suggests that the slope of the slide plane was at most a few degrees, indicating that a massive volume of material dislocated very rapidly, allowing the mass to build momentum. In the upper plate, gently tilted, allochthonous block masses with well-preserved internal strata are found. Further, the base of the slide is marked by a prominent planar shear above a thin basal breccia with clastic dikes extending upward into upper plate rocks. Where the basal plane is exposed, allochthonous upper plate rocks are sheared or intensely brecciated and pseudotachylyte has also been discovered along secondary shear planes (Hacker et al., 2014).

Interpretation of these findings indicate that the upper plate moved as a single unit, maintaining coherence of the internal strata, that slid along a basal shear zone marked by brecciation and brittle fracture extending variably upward into the upper plate (Biek et al., 2019). Elevated fluid pressures within the shear zone cause clastic dikes to extend upward. Pseudotachylyte is hypothesized to have formed towards the toe of the slide as the mass was coming to a halt and frictional heating occurred (Hacker et al., 2014; Biek et al., 2019). These features have also been documented in other large scale catastrophic rockslides (e.g. Anders et al., 2000; Weidinger et al., 2014) and support the interpretation of these slides as single emplacement events.

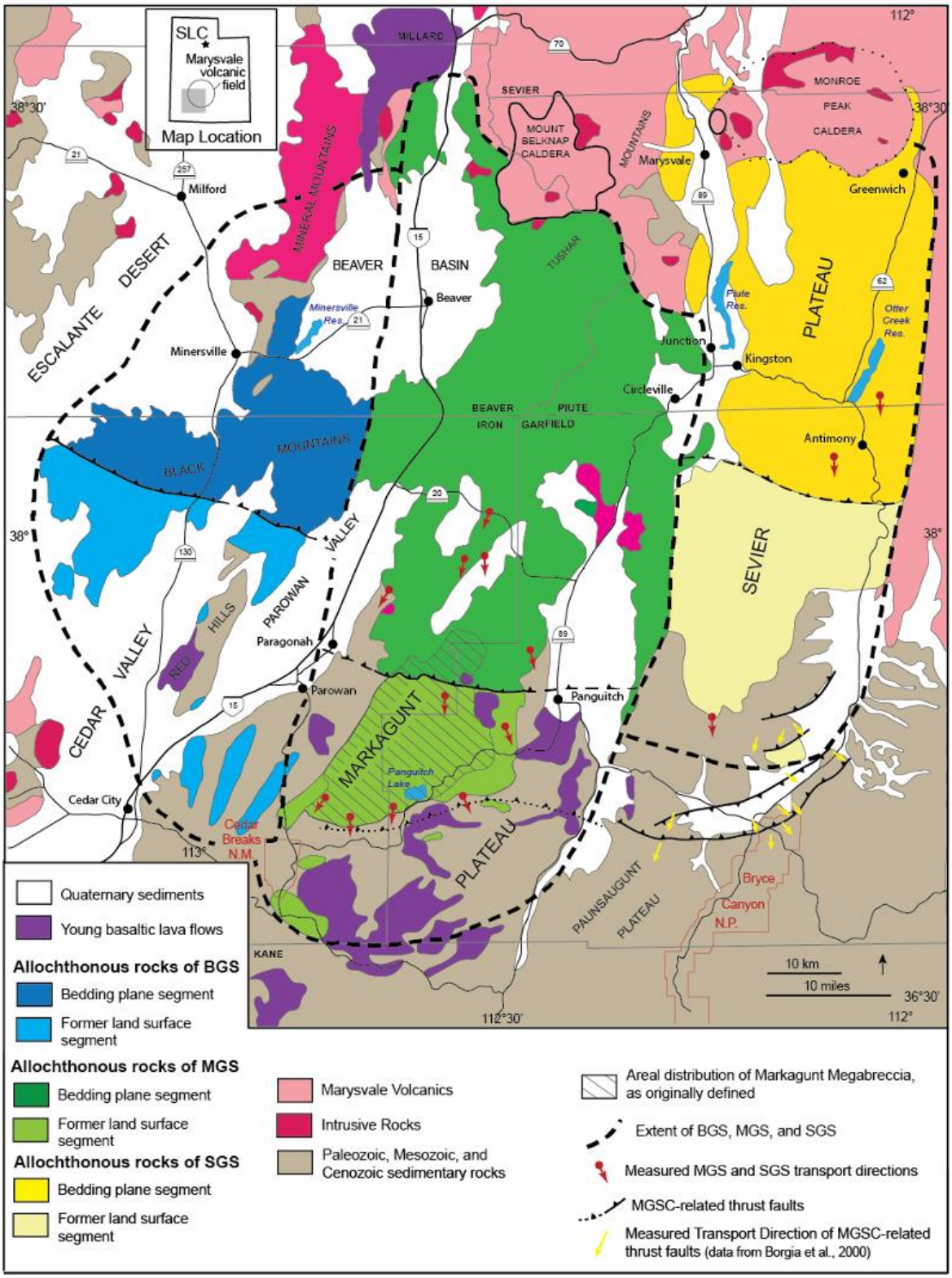

Figure 1: Schematic geologic map of the southwest portion of the Marysvale Volcanic Field in southwest Utah. The area of interest is located on the right side of the figure, notably the Sevier Plateau. The Monroe Peak Caldera is shown in the top right and the projected ramp fault is shown near Antimony. (Biek et al., 2019).

Stratigraphy

At the time of the slide in the Oligocene, the stratigraphy of the area was dominated by Marysvale volcanic units underlain by pre-volcanic sedimentary layers (Biek et al., 2019). At the surface was the massive volcanic Mt. Dutton Formation, including various subparts, the Kingston Canyon Tuff member and limited lateral extent of the Isom Formation and Bear Valley Formation. These Marysvale volcanic rocks overlay the Brian Head Formation and the Claron Formation (Hacker et al., 2014). A pre-slide schematic cross section is shown in Figure 4.

The Mt. Dutton formation is a massive unit made of intertonguing and cross cutting vents sourced from surrounding stratovolcanoes. Lithology of the Mt. Dutton is andesitic to dacitic mudflow breccia and interbedded conglomerate and tuffaceous sandstone. (Anderson and Rowley, 1975). Sub-member Kingston Canyon Tuff stands out within the massive Mt. Dutton as a densely welded vitrophyre layer, hypothesized to potentially have acted as seal layer trapping high fluid pressures in the basal sliding surface throughout the slide (Braunagel et al., 2020). Sub-member Bear Valley is a sandstone unit within the Mt. Dutton. (Biek et al., 2019).

The Brian Head Formation is estimated to be deposited 33-37 Ma (Biek et al., 2019), ranges in thickness up to 300 m, and marks the beginning of pre-Marysvale volcanic rocks. (Hacker et al., 2014). The Brian Head is a structurally weak layer beneath the Marysvale volcanic zone, composed of clay and ash rich tuffaceous sediments.

Due to its weak properties relative to the surrounding units, the top of the Brian Head has been proposed as the detachment surface in slide initiation (Hacker et al., 2014, Biek et al., 2019). While it is known lithologically to be structurally weak, quantitative data for the frictional strength is unknown. One objective of the ongoing project on the SGS is to measure the frictional properties of the Brian Head. The model in this project treats the top of the Brian Head Formation as the potential detachment surface, and idealizes unknown mechanical properties, and the shape, with the intention of being further refined by ongoing work.

The Claron Formation underlies the Brian Head Formation along a conformable sedimentary contact. The Claron is made of conglomerate, sandstone, and limestone, accumulated in a fluvial and lacustrine environment. (Hacker et al., 2014, Biek et al., 2019). The Claron Formation is found throughout the SGS field area in the lower-plate rocks, below the basal surface.

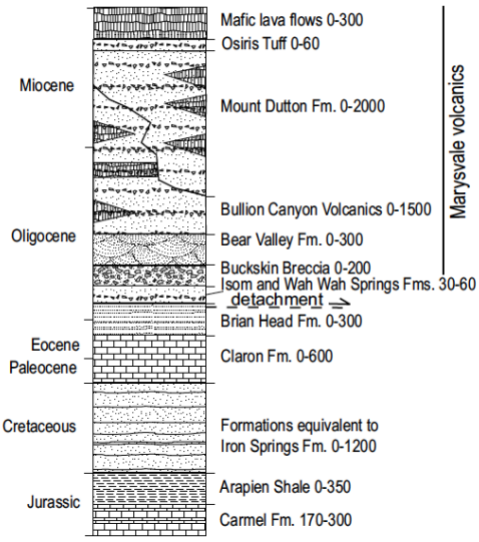

Figure 2: Simplified stratigraphic column of Marysvale volcanic units displaced by the Marysvale Gravity Slide Complex. Thickness for each unit is shown in meters. This figure comes from a paper on the Markagunt Gravity Slide, adjacent to the Sevier Gravity Slide. Much of the stratigraphy remains the same for both sides although the lateral extent of some formations is limited to the MGS. This stratigraphic column notably does not include the Kingston Canyon Tuff sub-member of the Mt. Dutton Formation. Figure taken from Hacker et al., 2014.

Landslide Classification

Landslides occur across in a large variety of geologic settings. One common classification of landslides (Varnes, 1978) sorts slides by type of material and movement (Table 1). Materials are classified as bedrock or engineering soils, i.e., granular materials. In terms of movement, landslides are considered one of the following: falls, topples, slides, spreads, and flows. Falls describe detachments with little to no shear displacement (Figure 3D), while topples are similar, yet distinctly rotate about a pivot point (Figure 3E). True slides are characterized both by shear strain and displacement along a sliding surface with an upper and lower block (Figure 3A, B, C). Spreads describe movement of lateral extension accommodated by fractures (Figure 3F), and flows can be unconsolidated material or "creep" of bedrock (Figure 3G) (Varnes, 1978).

Table 1: Classification of Landslides, both by type of movement and type of material. (Varnes, 1978)

TYPE OF MOVEMENT		TYPE OF MATERIAL		
		BEDROCK	ENGINEERING SOILS	
			Predominantly coarse	Predominantly fine
FALLS		Rock fall	Debris fall	Earth fall
TOPPLES		Rock topple	Debris topple	Earth topple
SLIDES	ROTATIONAL	Rock slide	Debris slide	Earth slide
	TRANSLATIONAL			
LATERAL SPREADS		Rock spread	Debris spread	Earth spread
FLOWS		Rock flow (deep creep)	Debris flow (soil creep)	Earth flow
COMPLEX		Combination of two or more principal types of movement		

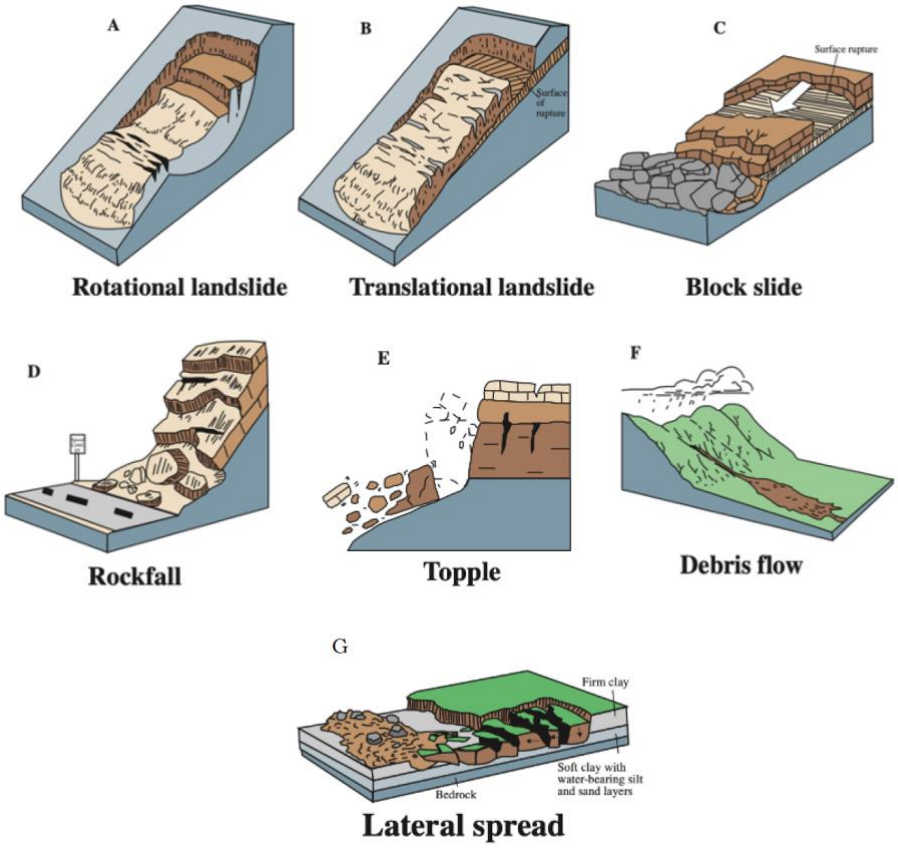

Figure 3: Schematic examples of various slide types. True slides, rotational and translational, in A and B. Block slide, C, is another example of a true translational slide. Rockfalls are represented in D, topples in E, flows in F, and lateral spreads in G. (Highland, 2004, USGS Fact Sheet).

In terms of this traditional classification scheme, the SGS is classified as a rock slide, representing true slide motion with bedrock material. The SGS is a true slide as shear strain and displacement is present and localized along a basal sliding surface. While Varnes (1978) further classified true slides as either rotational or translational, the SGS exhibits properties of both. Rotational slides, commonly thought of as slumps, indicate rotational motion in the slide material due to concavity in the detachment surface (Figure 3A). Translational slides have more or less planar detachment surfaces (Figure 3B). In the SGS, we see both of these characteristics. This ambiguity is in large part due to the massive scale of the structure, which does not fit neatly into a traditional classification scheme. Whereas the slide initiated on a planar detachment surface, the depth of the detachment surface was likely as deep as 2-3 km, requiring formation of the ramp for the detachment to reach the surface in a process described by Fleming and Johnson (1989) and Martel (2004) and illustrated in Figure 4.

Controlling Parameters of Slide Initiation

All landslides are unified in that they all involve failure of material under shear stress (Varnes, 1978). Failure requires that the shear stress exceeds the frictional strength of the material.

The shear stress along any potential detachment surface is primarily controlled by the surrounding state of stress. Local stress perturbations are driven by a number of factors. Topographic overburden and steep slopes increase stress perturbations caused by distortions in the uneven free surface above. Magmatic intrusions such as dike injections can increase lateral pressure resulting in increased tractions along the detachment zone. Other tectonic and fault driven processes can act to influence local stress perturbations as well (Varnes, 1978).

The frictional strength of the material is controlled by the mechanical properties of the material, such as the Young's modulus, Poisson's ratio, density, etc., but also can also be influenced by outside factors. Elevated pore fluid pressure within the material decreases the effective normal stresses throughout and thus the frictional strength of the rock (Hubbert and Rubey, 1959).

Again, for any given landslide, initiation involves failure under shear stress, and thus is driven by processes that act to increase the shear stress along a detachment surface, or that act to decrease the frictional strength of the material along that surface.

Application to SGS

To analyze initiation of the SGS, I am interested in exploring the shear tractions resolved along the detachment surface, representing the Brian Head Formation. This analysis will be complementary to ongoing work in the collaborative project on the SGS which will determine the physical properties of the slide-related rocks, namely the frictional strength of the Brian Head Formation. These two complementary pieces will provide deep insights into the catastrophic failure and emplacement of the SGS.

To accomplish this analysis, I will model the stress distribution beneath an uneven topography representing pre-slide conditions of the SGS. Stress distributions beneath topography are used to calculate shear tractions along the Brian Head Formation. This analysis is possible using the framework of linear elastic fracture mechanics. Since the concentration of displacements in a landslide happens across a surface that is very thin compared the dimensions perpendicular to slip, landslides may be analyzed using fracture mechanics, idealized as initiating on an infinitesimally thin shear fracture (Martel et al., 2003). Martel et al. (2003) illustrates how an elastic model of a shear fracture can provide insights into the initiation of sliding along a weak surface. Modeling in this paper follows this framework and treats the Brian Head Formation as a shear fracture along which we calculate resolved shear and normal stresses due to topographic perturbations. Because of theory that landslides initiate when the shear stress exceeds the frictional strength, we can use these calculated shear stresses to assess detachment potential.

Potential Triggering Events

While the focus of this thesis is to establish the contribution of the slope geometry and far field stresses on instability of the SGS, there are several additional factors that could, if superimposed on the static topographic stresses, bring the slope closer to failure and trigger a slide. None of these factors are considered explicitly in my model but are important to consider in the larger scheme of the problem and will be discussed in light of the results. Again, these events are hypothesized as triggers because they act to increase the shear stress or decrease the frictional strength along the detachment zone.

One process that may have driven initiation is lateral spreading. Lateral spreading in the substrata is a process by which localized extension and thinning in the subsurface causes increases in differential stresses. Thus, stress perturbations within the body are further exaggerated and landslides may initiate at the surface (van Wyk de Vries and Francis, 1997). Within the SGS region, lateral spreading very well may have occurred, driven by movement along the Ruby's Inn thrust fault (Biek et al., 2019). The Ruby's Inn thrust fault is part of the Paunsaugunt thrust fault system in southern Utah as shown in Figure 1 and Figure 4. This thrust system resulted from gravitational spreading of the Marysvale field prior to the slides. Lateral, north-south, spreading in this region may have increased shear stress and induced failure (Merle et al., 1993; Hacker et al., 2014; Biek et al., 2019).

Another process that may have driven increases in shear stress is the growth of magmatic chambers stemming from the volcanic field. Biek et al. (2019) suggest that inflation of the volcanic pile from either a batholith underlying the heart of the volcanic field, or laccolith intrusions above the batholith could have tilted the volcanic strata gently, providing the perfect slope for the massive slide. Moreover, intrusions can exert lateral stresses, driving lateral spread in the subsurface and related slope destabilization. This is represented in Figure 4 as the black shaded area. Moreover, magmatic intrusions within the volcanic field would increase stress perturbations in an expanding ridge.

Finally, the role of pore fluid pressure in slide mobility is currently being studied. It is becoming clear that fluid pressure played an important role in the mobility of the slide (Braunagel et al., 2020). While it is yet unclear if fluid pressure directly influenced initiation of the slide, the presence of highly pressurized fluid in the mobility of the slide indicates that fluid pressure may have influence initiation as well.

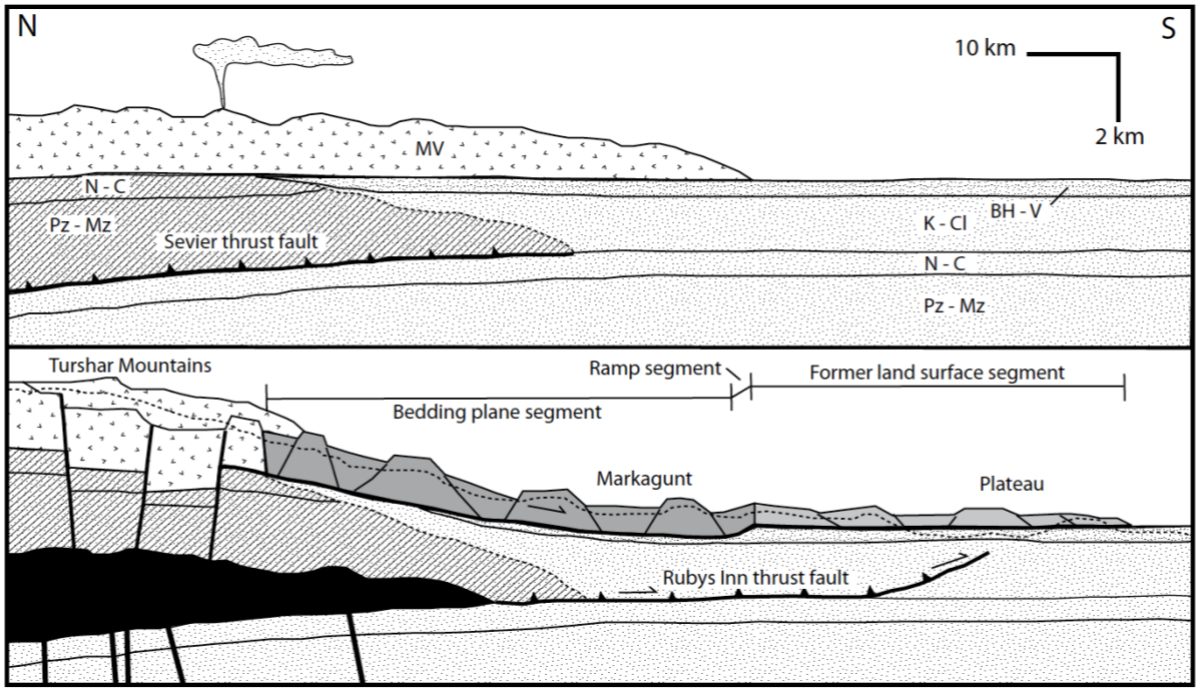

Figure 4: Schematic north-south cross section of Markagunt Gravity Slide, before and after sliding. Hacker et al. (2014) hypothesize that magmatic intrusions, shown in black, took advantage of the Sevier thrust fault, inflating the volcanic pole and driving lateral spread along the Ruby's Inn thrust fault. Pz-Mz – Paleozoic and Mesozoic sedimentary rocks; N-C – Jurassic Navajo Sandstone and Carmel Formation; K-Cl – Cretaceous and Claron Formation sedimentary rocks; BH-C Brian Head Formation and oldest regional ash flow tuffs; MV – Marysvale volcanics. Dashes lines represent erosion surfaces during Sevier thrusting. (Hacker et al., 2014).

METHODS

Modeling Framework

Modeling and analysis of the initiation of the SGS in its full complexity requires an understanding of the stress distributions in the paleo-environment as well as incorporating potential trigger events. In a completed version, beyond what I accomplish here, the model will solve for stress distributions beneath a given topography and simulate its relationship with potential triggering factors over time to analyze the initiation of the slide and the size of the incipient failure zone.

The goal of my contribution to this larger project is to analyze parameters of pre-slide conditions and their influence on slope stability and the size of the potential detachment surface, before considering other triggering events.

Variables, constants, and stress transformations used to calculate outputs are shown in Table 2. Parameters analyzed are the far field stresses, the vertical extent of topography in the Marysvale region pre-slide, and the frictional strength of the potential detachment surface. Material properties, i.e., Young's Modulus and Poisson's ratio, the constitutive behavior, the general geometry of topography, and the depth to the detachment surface assume given input values in the model and will be subject to further refinement in future work on the SGS. The model generates results of subsurface stress distributions used to evaluate slope stability by analyzing stresses to two failure criteria. In doing so, I establish a relationship between the model parameters, topography and far field stresses, and the inferred length of the detachment zone.

Table 2: Constants, parameters, and stress transformations throughout the model. See text definitions for individual variables and constants.

Constants	Young's Modulus, E (*MPa*)	Poisson's ratio, ν	Density (*kg m^{-3}*), ρ	Acceleration due to gravity (*m s^{-2}*), g	Tectonic Load, T (*MPa*)	Number of elements, n
	30,000	0.25	3,000	10	-10	500
Parameters	Far Field Stresses Vary between Equations (4a), (4b), and (4c)		$\sigma_{yy} = \rho g y,$ (3) $\sigma_{xx} = \sigma_{yy},$ (4a) $\sigma_{xx} = \frac{\nu}{1-\nu}\sigma_{yy},$ (4b) $\sigma_{xx} = \frac{\nu}{1-\nu}\sigma_{yy} + T,$ (4c)			
	Topography Vary h and k in Equation (1)		$f(x) = \frac{h}{1+e^{k(x-x_o)}}$ (1)			
Results	Stress Distribution Calculated for observation grid beneath topography.		$[A_{ij}][X_i] = [B_j]$ (5) $[A_{ij}{}^{obs}][X_i] = [\boldsymbol{\sigma_{ij}^{obs}}]$ (6)			
	Normal and Shear Stress Calculated along potential detachment surface.		$\boldsymbol{\sigma_n} = \sigma_{y'y'} = \sigma_{xx}\sin^2(\theta) + \sigma_{yy}\cos^2(\theta) - \sigma_{xy}\sin(2\theta)$ (7a) $\boldsymbol{\sigma_s} = \sigma_{x'y'} = \frac{1}{2}(\sigma_{yy} - \sigma_{xx})\sin(2\theta) + \sigma_{xy}\cos(2\theta)$ (7b)			

Formulation of the Problem

I implement a Boundary Element Method (BEM) approach described by Martel and Muller (2000) in MATLAB and apply it to the initiation of the SGS. As described in greater detail below, I treat the far field stress state and the geometry of the topographic surface as independent variables in the simulations and examine the resulting stress distributions beneath the surface.

The modeling process is based on the Displacement Discontinuity Method (DDM) outlined by Crouch and Starfield (1983) and calculates the stress distribution in the subsurface as a function of stress perturbations driven by the topographic surface and far field stresses (Martel and Muller, 2000; Griffith, 2014). Within the DDM, the surface in the model, the topography, is defined as n linear elements, where each element is treated as a crack. Each element of the boundary has a constant displacement discontinuity which is calculated based on the boundary conditions set. The displacements across each element are then related the resultant stress at surrounding observation points.

The BEM formulation of the DDM calculates the change in stress due to a complex boundary by simultaneously solving a system of equations that relate the displacement along each element to the stress changes in the surrounding medium. So, the model approach simulates the mechanical interaction between the elements of the boundary and the model domain. Figure 5 shows the conceptual model of the BEM formulation for deriving gravitational stresses under an irregularly eroded topographic surface. Gravitational stresses are calculated for an infinite body from which the stresses of the overburden section, above the topographic surface, are subtracted, leaving the stresses below any input topography. The topography is the only boundary surface considered in the model. The boundary conditions are set such that the normal and shear stresses along topography remain zero, and farther from the surface, stresses approach the far field stresses.

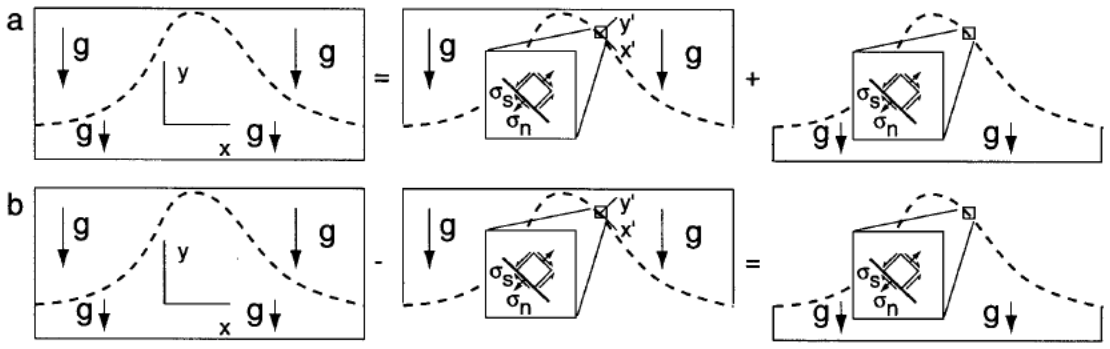

Figure 5: Conceptual model showing how an infinite body (left) with gravitational stresses can be broken into two parts (center and right). In (b) it is shown that that the gravitational stresses imposed on the overburden (center) can be subtracted from the infinite body (left) to find the stresses under any given topography (right). Image from Muller and Martel, (2000).

Topographic Surface

The boundary defined within the model is the paleo-topography. This surface is defined as a simplified schematic of the paleo-land surface, rising in elevation toward the volcanic field to the north, and falling to a sub-horizontal plane to the south. This surface is treated as a free surface, meaning no normal or shear stress act on the surface.

The surface is defined by a logistic function, resembling an "S-shaped" curve that flattens at either end. This function is ideal to input topography because it is simple to manipulate and create varying topography. The parent function of the logistic function is defined as follows:

$$f(x) = \frac{h}{1 + e^{k(x - x_o)}} \qquad (1)$$

In Equation (1), h is defined to be the total change in elevation, k is rate variable that controls the length over which the elevation h is lost, and x_0 is the inflection point of the function. These three variables control the shape of the logistic function (Figure 6), and mapping data can be used to estimate these values for the paleo-land surface. In reference to Figure 1, the ramp fault on the Sevier plateau represents the estimated base of the volcanic ridge (Biek et al., 2019). Therefore, k and x_0 can be constrained such that the top of the ridge is $x = 0\ km$, and the base of the ridge is at $x = 45\ km$. I take $k = 0.0001$, $x_0 = 25000$. But h, the height of the volcanic pile, is yet unknown. Therefore, I take h to vary by increments of 5 kilometers, up to 20 kilometers.

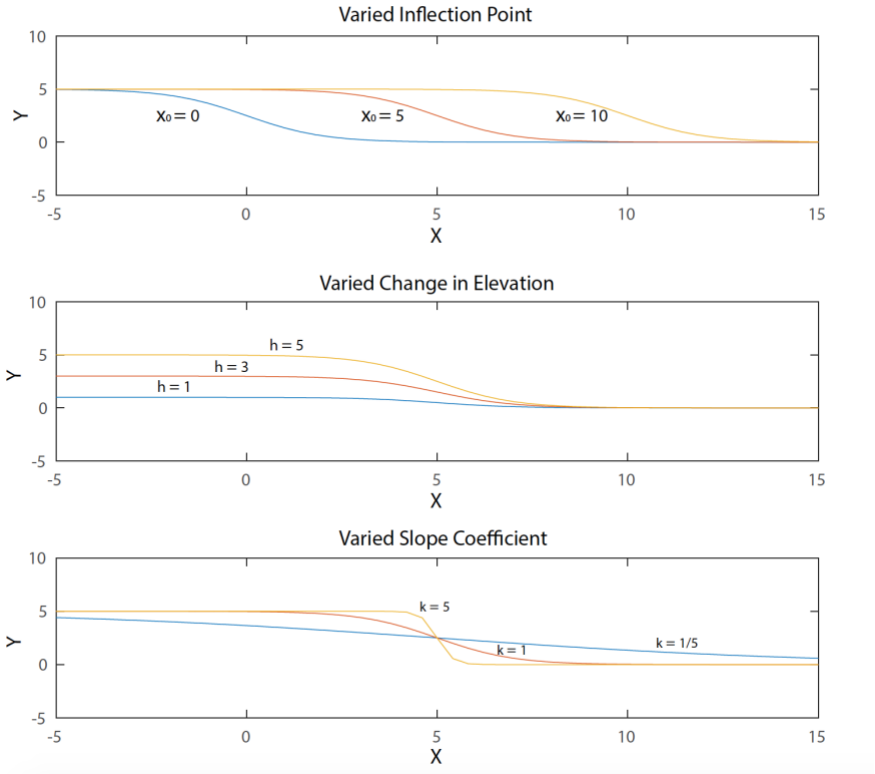

Figure 6: Characteristics of the Logistic function, Equation (1), shown as each of its components are varied. The inflection point is varied, shown in horizontal translations (top). The numerator term, h, is varied representing how topographic relief is varies (middle). The slope coefficient, k, is varied finally (bottom). These three elements control the shape of the logistic function, used to represent topography.

Far Field Stress

As stated previously, the true regional state of stress at the time of slide initiation is unknown. Therefore, in my model, far field stresses vary over three endmember stress regimes, isotropic, lateral extension, and lateral compression. Far field stress definitions in the model are derived from Muller and Martel (2000).

In the process outlined by Muller and Martel (2000), far field stresses are initially taken to be defined by gravitational stresses acting on the Earth, which is treated as a laterally confined body with a horizontal traction free surface (i.e., horizontal topography) and horizontal displacements are zero. The stresses that arise from the gravitational body forces in this situation are (Jaeger and Cook, 1979):

$$\sigma_{yy} = \rho g y, \qquad (2a)$$

$$\sigma_{xx} = \frac{\nu}{1-\nu}\,\rho g y, \qquad (2b)$$

$$\sigma_{xy} = \sigma_{yx} = 0, \qquad (2c)$$

Here ρ is the density of the material, g is the acceleration due to gravity, ν is Poisson's ration, and y is the depth. These equations are used to calculate the far field stresses which remain unchanged regardless of local variations in topography. It is important to note that this is for a laterally confined body, free of any tectonic activity.

In my model, Equation (2b) is modified to include varying amounts of tectonic activity which defines our three endmembers. Far field stresses are defined in the model as follows:

$$\sigma_{yy} = \rho g y, \qquad (3)$$

$$\sigma_{xx} = \sigma_{yy}, \qquad (4a)$$

$$\sigma_{xx} = \frac{\nu}{1-\nu}\,\sigma_{yy}, \qquad (4b)$$

$$\sigma_{xx} = \frac{\nu}{1-\nu}\,\sigma_{yy} + T, \qquad (4c)$$

In an isotropic state of stress, vertical and horizontal stresses are equal to each other throughout the body, described in equations (3) and (4a).

Lateral extension describes a critically stressed body within classical Andersonian normal faulting regime, where vertical stress is greater than horizontal stress. Extension is described in equations (3) and (4b) for a laterally confined body and is derived from equations (2a) and (2b).

Lateral compression, the opposite of extension, describes a critically stressed, Andersonian thrust system, where horizontal stress exceeds vertical stress. Compression is described by equations (3) and (4c). Equation (4c) is derived from (2b) with an extra term for added horizontal tectonic load, T, defined such that minimum horizontal stress is larger than the maximum vertical stress.

Coordinate System, Variables, and Constraints

I follow the setup of Martel and Muller (2000), y-axis as vertical, positive up, and the x- and z-axes are North-South and East-West horizontal axes, respectively. The slide direction then is along the x axis, and therefore interest lies in stresses along the x-axis cross section of the area and not on the z-axis. For these purposes, we assume that two-dimensional cross section which is analyzed (Figure 4) is representative of a 3-D structure in which z extends in both directions. Thus, I assume plane strain deformation, in which the deformation in the z-axis is equal to zero and confine the analysis to two dimensions, the x and y directions.

Calculating Stress Distribution Results

Results include a complete stress distribution (σ_{yy}, σ_{xx}, and σ_{xy}) beneath the topographic surface as well as the normal and shear stress components (σ_n and σ_s) along the potential detachment surface. These results are calculated using the Displacement Discontinuity Method and Boundary Element Method.

Matrix equations for BEM summarized by Martel and Muller (2000) are shown below:

$$[A_{ij}][X_i] = [B_j] \qquad (5)$$

$$[A_{ij}{}^{obs}][X_i] = [\sigma_{ij}{}^{obs}] \qquad (6)$$

Our model relies on the principle of superposition to solve for the displacement discontinuities for each element, $[X_i]$, as described in Equation (5). Using the boundary conditions, $[B_j]$, and a coefficient matrix $[A_{ij}]$, displacements are calculated. (Crouch and Starfield, 1973; Martel and Muller, 2000)

Once the displacements, $[X_i]$, are solved for, they can be used to calculate stress and displacements at a set of observation points, such as those on a regular grid or a subset of points along the detachment surface. A new coefficient matrix, $[A_{ij}{}^{obs}]$, is calculated, and the stress distribution, $[\sigma_{ij}{}^{obs}]$, is calculated by multiplying the coefficient matrix by the displacements, as described in Equation (6) (Martel and Muller, 2000).

In the model, the boundary of the body, the topographic surface, is approximated by a series of individual line segment elements. Boundary conditions, σ_n and σ_s, are specified for each for each element along the boundary. In our case, the boundary conditions are set that the topographic surface is a free surface, maintaining zero normal and shear stresses. These boundary conditions are represented by the matrix $[B_j]$.

For the total stress distribution, observation points are set up as a grid spanning the modeling domain below topography The local, topographically driven stresses calculated in Equation (7) for the gridded observation points are superimposed onto the far field stresses used in Table 1 to yield a traction free topographic surface with a complete stress distribution beneath.

Stability Criteria

Derived from the resulting stress distributions in the subsurface, two stability criteria are used to analyze potential failure along the detachment surface. First, normal and shear stresses are calculated directly for an idealized Brian Head Formation as the potential detachment surface, and shear

stresses are analyzed against shear failure criterion. Secondly, a stability measurement ϕ is calculated, derived from the differential stress relative to the mean stress.

To analyze the normal and shear stress along the detachment surface, a second group of observation points are defined to approximate the potential detachment surface. The observation points follow parallel to the topography, 2 kilometers below the surface (Figure 7). The exact location of the Brian Head Formation, or the detachment surface more broadly, is unknown relative to paleo-topography, and idealizing the surface as parallel to topography is realistically unlikely. Ongoing study will refine the location of the detachment surface.

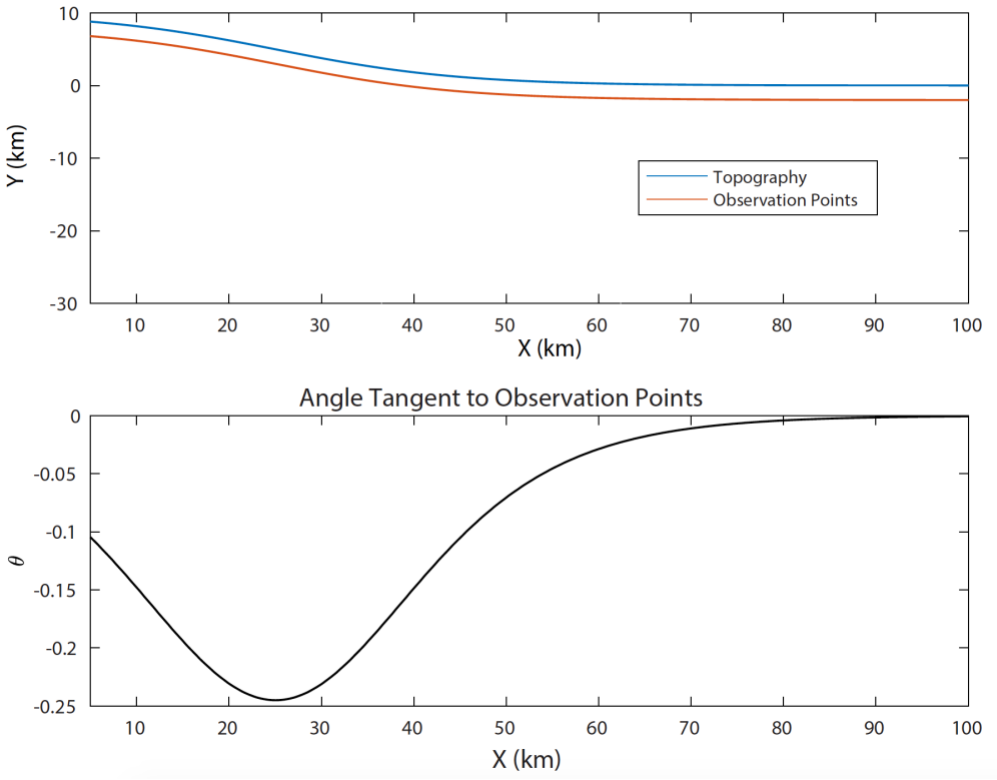

Figure 7: Top figure displaying topography in blue and observation points mimicking the potential detachment surface in red. Bottom figure shows the angle, θ, tangent to the observation points.

At each point, rotation transformations, shown in Equations (7a) and (7b), are used to transform previously calculated stresses σ_{yy}, σ_{xx}, and σ_{xy} into $\sigma_{y'y'}$ and $\sigma_{x'y'}$ (Turcotte and Schubert, 2014). Axes x' and y' are defined such that x' is tangent to the potential detachment surface and is offset from the original x axis by an angle of θ. The angle is calculated element by element, using the rise and run from neighboring points on each side.

$$\sigma_n = \sigma_{y'y'} = \sigma_{xx}\sin^2(\theta) + \sigma_{yy}\cos^2(\theta) - \sigma_{xy}\sin(2\theta) \qquad (7a)$$

$$\sigma_s = \sigma_{x'y'} = \frac{1}{2}(\sigma_{yy} - \sigma_{xx})\sin(2\theta) + \sigma_{xy}\cos(2\theta) \quad (7b)$$

$$\sigma_s^* = \mu_f \sigma_n \quad (8)$$

Using the concept of frictional strength, instability may be tested along the Brian Head Formation. Shear stresses calculated by the model are analyzed against critical shear stresses, σ_s^*, defined by the frictional strength μ_f, of the Brian Head. Critical stresses are defined in Equation (8). Since the true frictional strength of the Brian Head is unknown, the value is varied to analyze failure potentials for a range of strength values, $\mu_f = 0.1, 0.3,$ and 0.6. (Turcotte and Schubert, 2014). Calculated shear stresses along the detachment surface are analyzed against critical shear stress curves for various strength values.

Another measure of slope stability, ϕ, was developed by Iverson and Reid (1992) and is used in our model further inform stability analysis. ϕ is depending on the differential stress relative to the mean stress, and is defined as follows:

$$\phi = \frac{|\tau'_{max}|}{-\sigma'_m} = \frac{\sigma_1 - \sigma_3}{\sigma_1 + \sigma_3} \quad (9)$$

Above, σ_1 and σ_3 are the maximum and minimum principal stresses, $|\tau'_{max}|$ is the maximum shear stress or the differential stress, and σ'_m is the effective mean stress. ϕ is calculated throughout the initial observation grid over the entire stress distribution. When the differential stress is close to the mean stress, we expect instability. But when the differential stress is very low compared to the mean stress, we expect stable conditions. Therefore, values close to 1 indicate areas of instability while values close to 0 indicate stability. (Iverson and Reid, 1992).

Model Verification

Following the technique of Muller and Martel (2000), I check my model with a derived analytical solution introduced by Savage et al. (1985). To do this, I simplify my model to match the parameters, specifically the topographic surface and model domain, used by Savage et al. (1985) and Martel and Muller (2000) to check the solutions directly with their produced work.

One half of a laterally constrained symmetric ridge is considered with far field stresses imposed. The topography is simplified, running 4 m in length and losing 1 m of elevation. To follow the form of the literature, I plot $\sigma_{yy}, \sigma_{xx},$ and σ_{xy} under the ridge normalized by the term, $\rho g b$, where b is the height of the ridge, 1 meter (Savage et al., 1985; Martel and Muller, 2000).

RESULTS

Validation

Checking the model against the analytical solution provide by Savage et al. (1985) is done to validate the BEM model produced in the methods and provide confidence in the results moving forward. To check against the analytical solution, the topography and domain of the model were altered to match the system solved for by Savage et al. (1985) and reproduced by Martel and Muller (2000). BEM solutions calculated within my model are shown in Figure 8 and analytical solutions from the literature are shown in Figure 9. The fit is near perfect, validating the framework of the model built. Boundary effects are noted but are shallow enough to not interfere with further calculations and failure analysis.

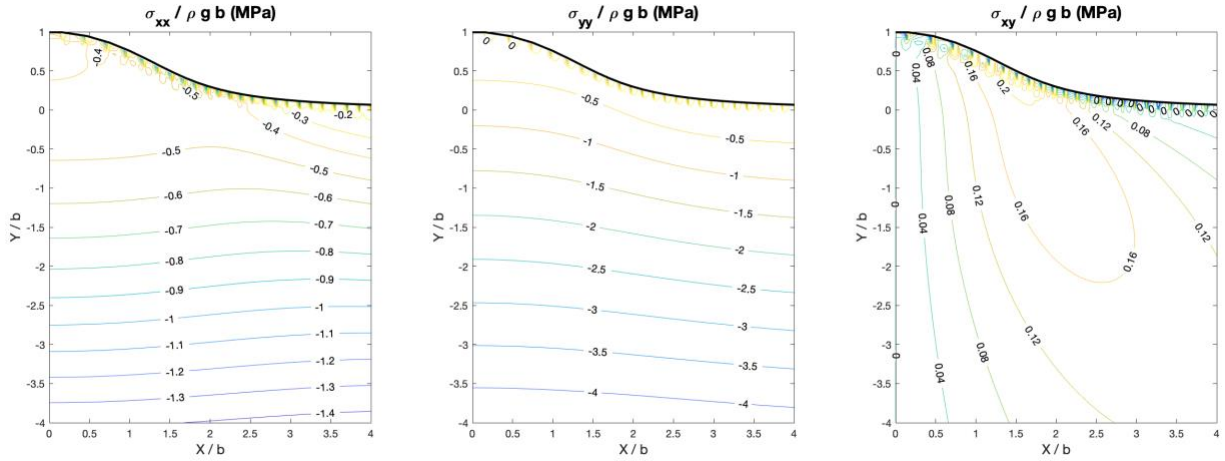

Figure 8: BEM solutions for a laterally constrained symmetric ridge, such that the curve is set equal the topography used by Savage et al. (1985). Stresses are normalized by a term $\rho g b$, where b indicates the height of the ridge. This normalization is done to match the figures produced by Savage et al., (1985). Horizontal stresses, σ_{xx}, are shown on the left, vertical stresses, σ_{yy}, in the middle, and shear stresses, σ_{xy}, on the right.

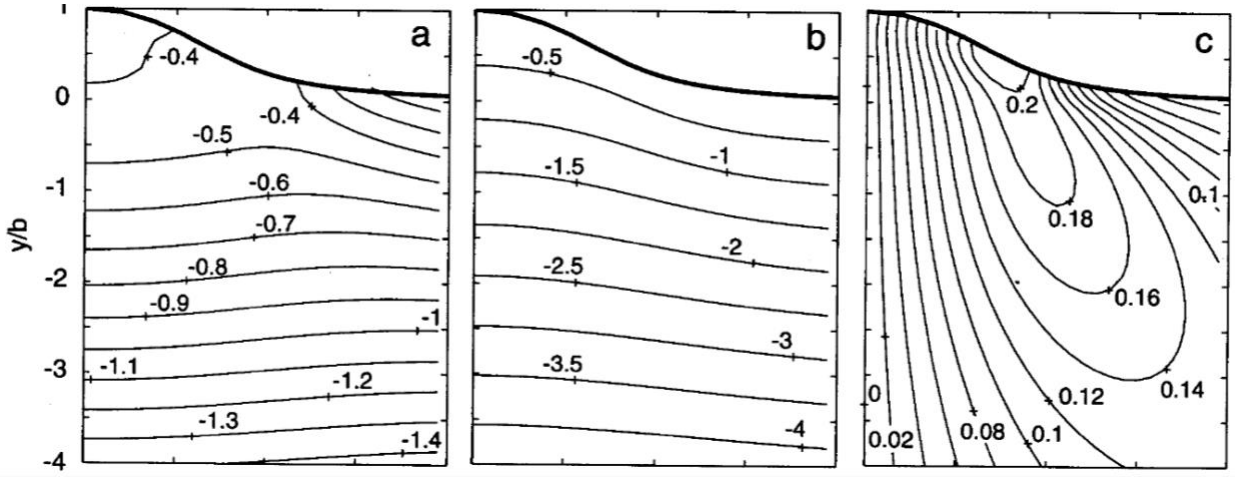

Figure 9: Analytical solutions for stresses below a laterally constrained symmetric ridge produced by Savage et al., (1985). Horizontal, vertical, and shear stresses are shown left to right, matching BEM figure. The vertical axis is normalized by the term b, which in our case is 1.

Stress Distributions for Varying Far Field Stresses

Stress distributions beneath topography are calculated for a variety of far field stresses while maintaining topographic geometry. Contour plots are shown for each stress component for each scenario to illustrate the complete 2D stress distribution beneath topography and that our model validates the boundary conditions.

Each figure below contains three subplots. The top showing σ_{yy}, the middle σ_{xx}, and the bottom σ_{xy}. The color bar on each side is in reference to stress in MPa. In this section, contour plots are shown for scenarios for the three stress regime endmembers while maintaining the topographic surface geometry. The topography is defined to have a total net change of elevation of 10 km and stress states shown are lateral compression $\sigma_h > \sigma_v$ (Figure 10), lateral extension $\sigma_v > \sigma_h$ (Figure 11), and isotropic stress $\sigma_h = \sigma_v$ (Figure 12).

Across all of the stress distributions the results validate the model formulation and our boundary conditions. In σ_{yy} and σ_{xx} distributions, stress perturbations are focused in the ridge and shallowly along the slope while contours trend subparallel to topography to the south and with increasing depth. σ_{xy} contours never trend subparallel to topography; they perturb away from the ridge. This illustrates the stress distribution as defined by the superposition of the far field stresses with topographically driven perturbances. σ_{yy} and σ_{xx} have nonzero far field components, which is not true of σ_{xy}. Thus, σ_{xy} distributions reflect solely the influence of the topographic perturbations and trends towards 0 away from the ridge, similarly σ_{yy} and σ_{xx} tend to contour subparallel to topography away from the ridge. Both of these occur because as distance away from the ridge increases, stresses tend towards the far field stresses, which for σ_{xy} is zero and for σ_{xx} and σ_{yy} is solely dependent on y.

Moreover, the distributions validate our boundary conditions. Within the distributions shown below, σ_{yy} and σ_{xy} can estimate normal stress and shear stress, respectively. As you approach the topographic surface, both values trend to zero, satisfying that the topography remains a free surface, maintaining zero normal and shear stress.

Compressional Stress Regime

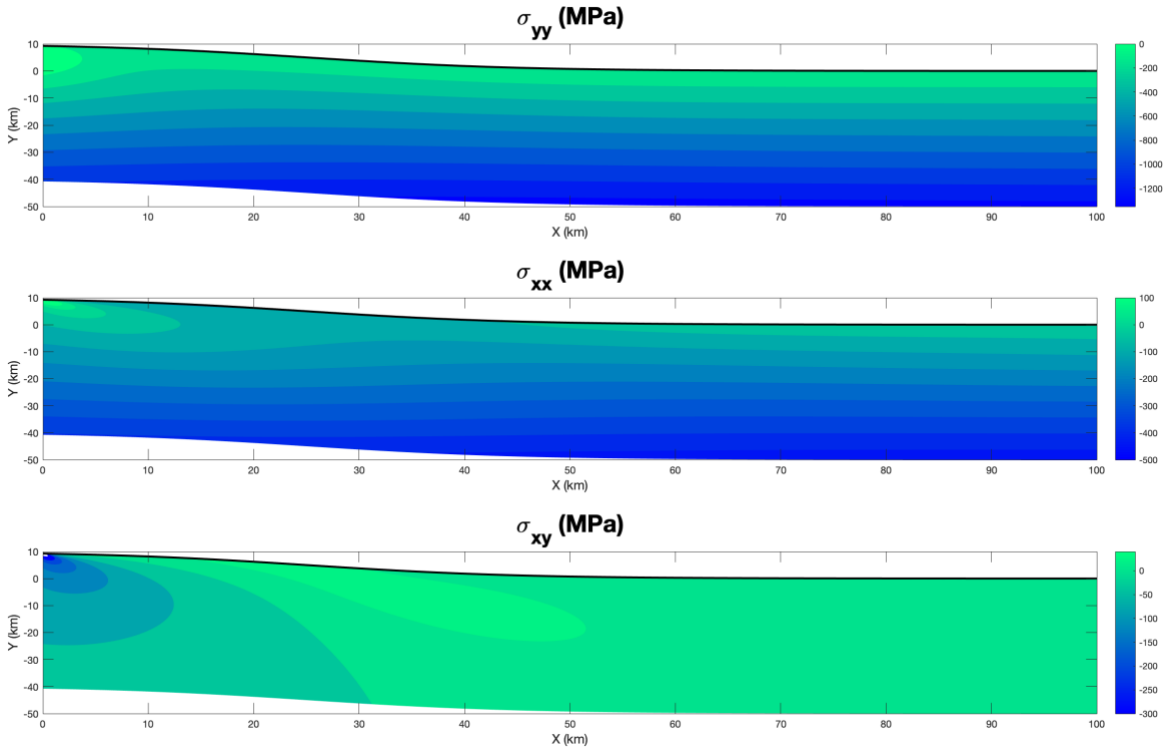

Figure 10: Stress Distribution for compressional stress regime, $\sigma_h > \sigma_v$.

Extensional Stress Regime

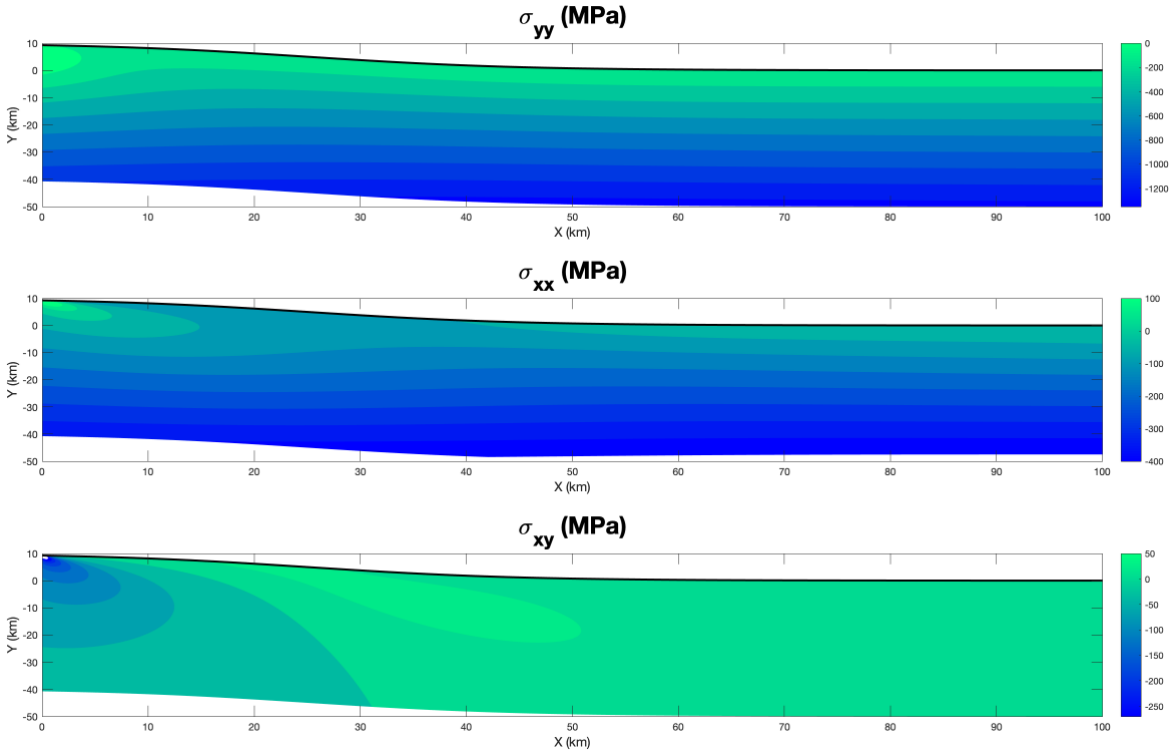

Figure 11: Stress Distribution for extensional stress regime, $\sigma_h < \sigma_v$.

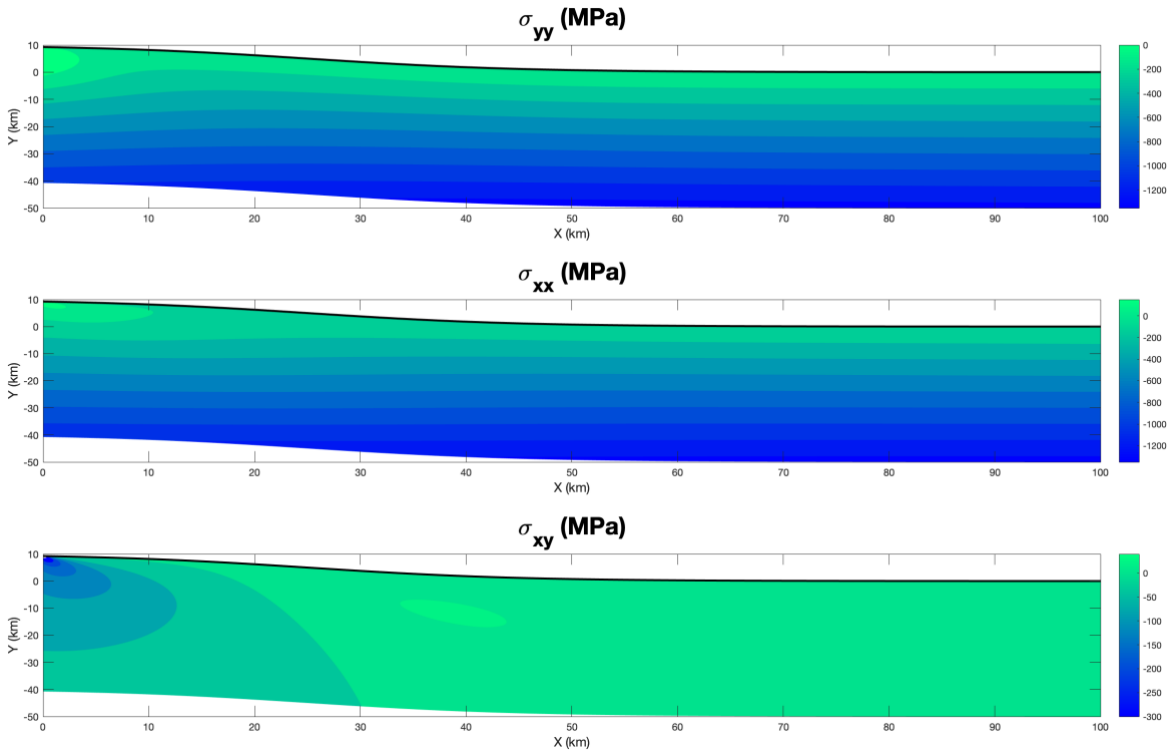

Figure 12: Stress Distribution for isotropic stress regime, $\sigma_h = \sigma_v$.

Stress Distributions for Varying Topography

Stress distributions beneath topography are also calculated for a variety of topographic surfaces while maintaining far field stresses. Contour plots are shown for each stress component for each scenario to illustrate the complete 2D stress distribution beneath topography and the influence of topography.

The figures below are of the same format as those above. The topography is defined for each figure, and three subplots for each stress component are shown for each topography. The regional stress state is of lateral extension, $\sigma_v > \sigma_h$ while the topographic surfaces are set to have a change in elevation of 5 km (Figure 13), 10 km (Figure 14), 15 km (Figure 15), and 20 km (Figure 16).

The distributions have the same underlying characteristics as those above, namely that far from the ridge stresses approach far field stress values, while normal and shear stresses trend towards 0 at the surface. More importantly, they illustrate the influence of topographic relief on stress perturbations beneath topography. As the change in elevation increases, stress perturbations extend farther from the ridge and are higher in magnitude, therefore both maximum differential stresses are increased, and the location of maximum differential stress migrates further down the ridge to the south.

Change in elevation = 5 km

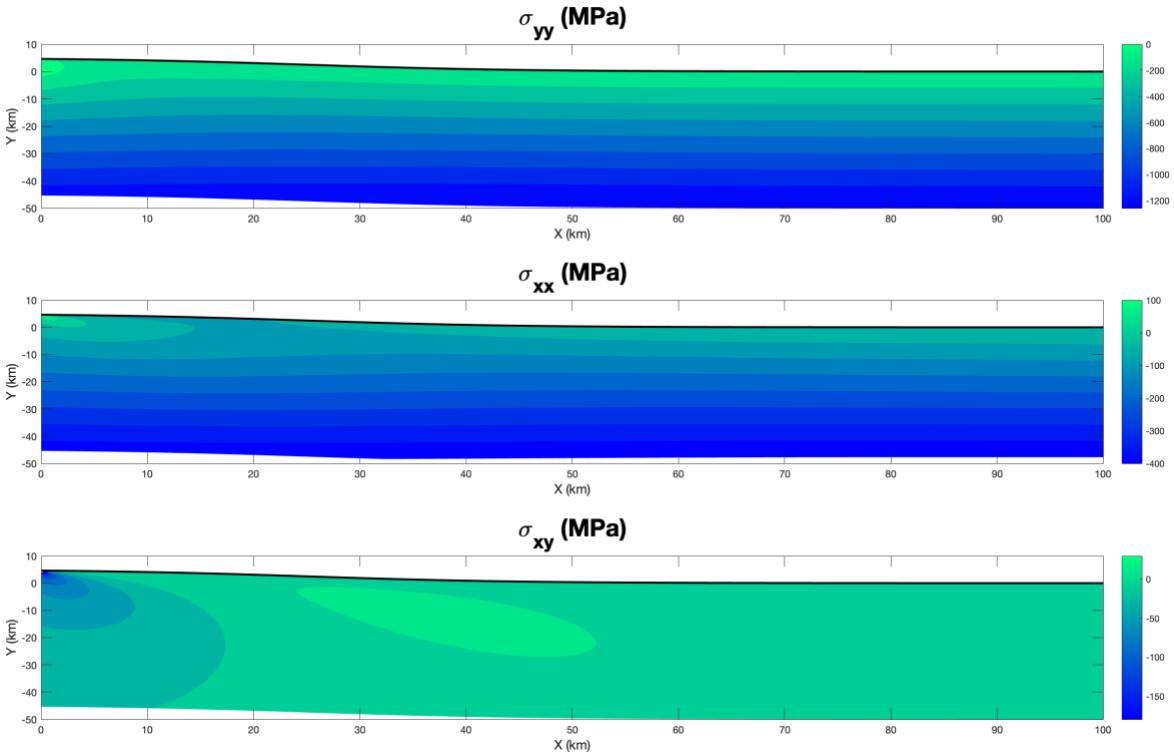

Figure 13: Stress Distribution for an elevation change of 5 kilometers.

Change in elevation = 10 km

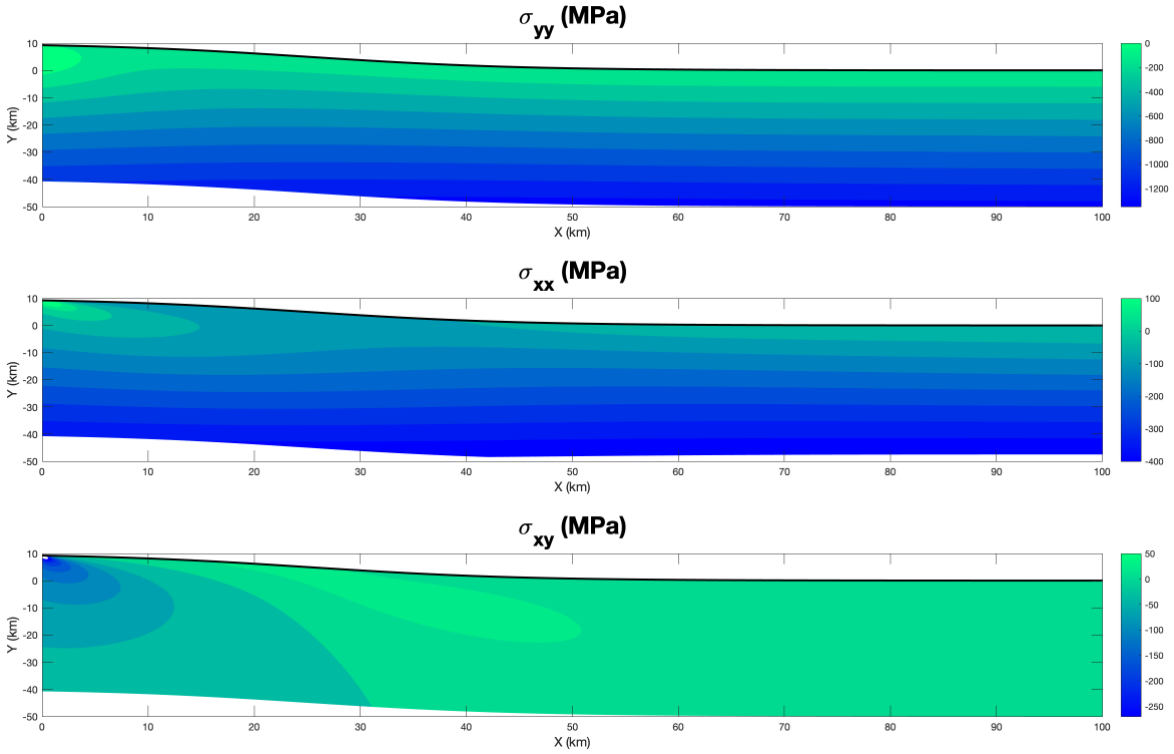

Figure 14: Stress Distribution for an elevation change of 10 kilometers.

Change in elevation = 15 km

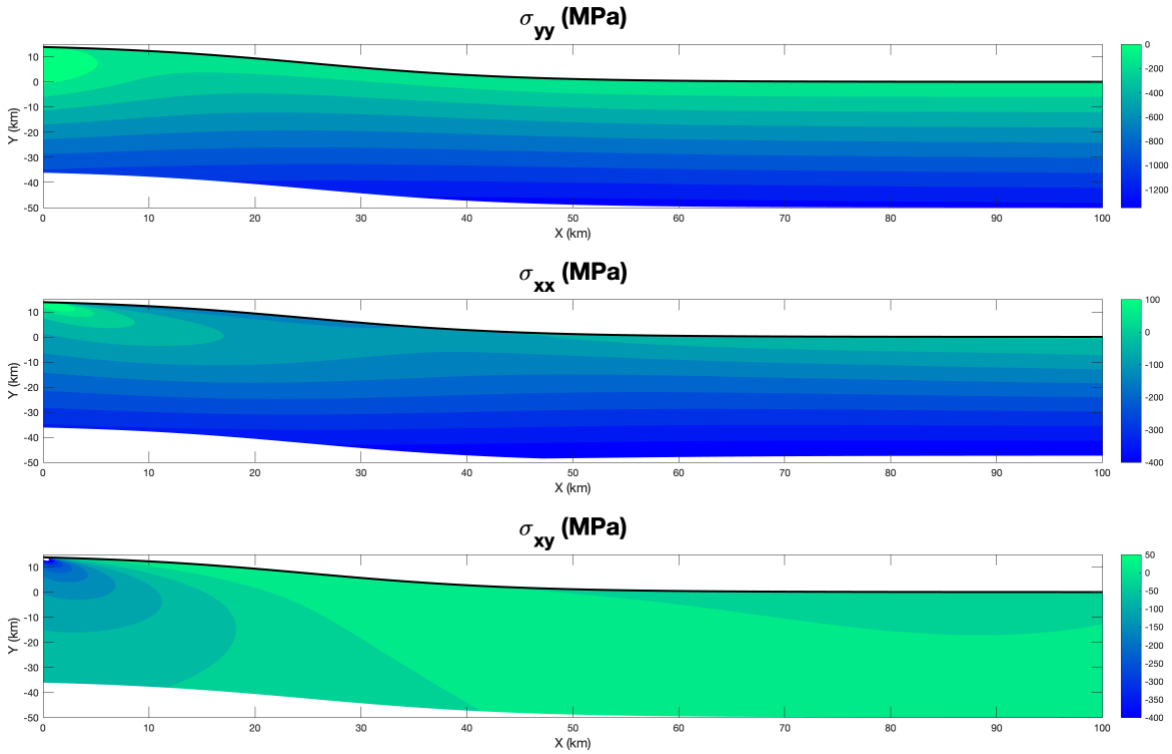

Figure 15: Stress Distribution for an elevation change of 15 kilometers.

Change in elevation = 20 km

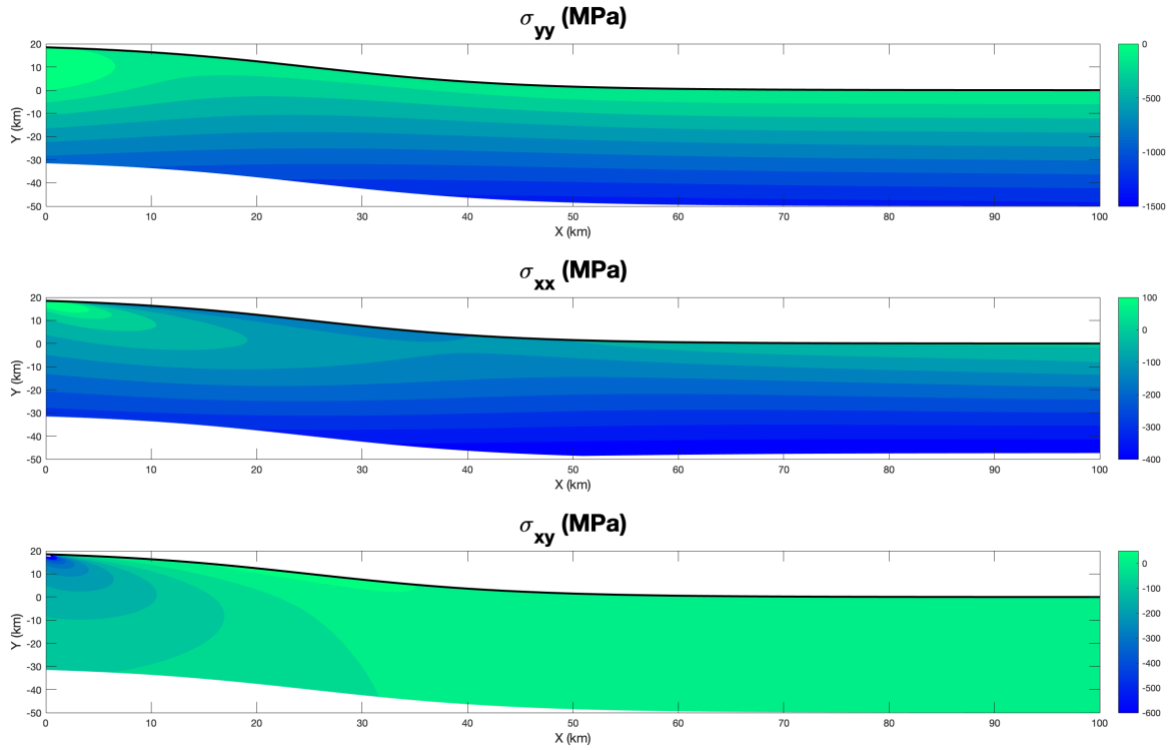

Figure 16: Stress Distribution for an elevation change of 20 kilometers.

Normal and Shear Tractions Along Potential Detachment Surface

Normal and shear stresses along the potential detachment surface are calculated based on the stress distributions for each stress regime and topography. Data are shown from trials run with the extensional stress regime, $\sigma_v > \sigma_h$, with varying changes in elevation (5, 10, 15, 20 km), represented by changes in the variable, *h,* in Equation (1).

Shear stresses, σ_s, for each trial (solid line) are plotted against the hypothetical critical shear stress curves, $\sigma_s{}^*$ (dashed lines). Places where the calculated shear stress exceeds the critical shear stresses indicates a potential zone of failure. Therefore, those areas of X for which $\sigma_s > \sigma_s{}^*$, are more likely to be areas of slope instability in the paleo-environment.

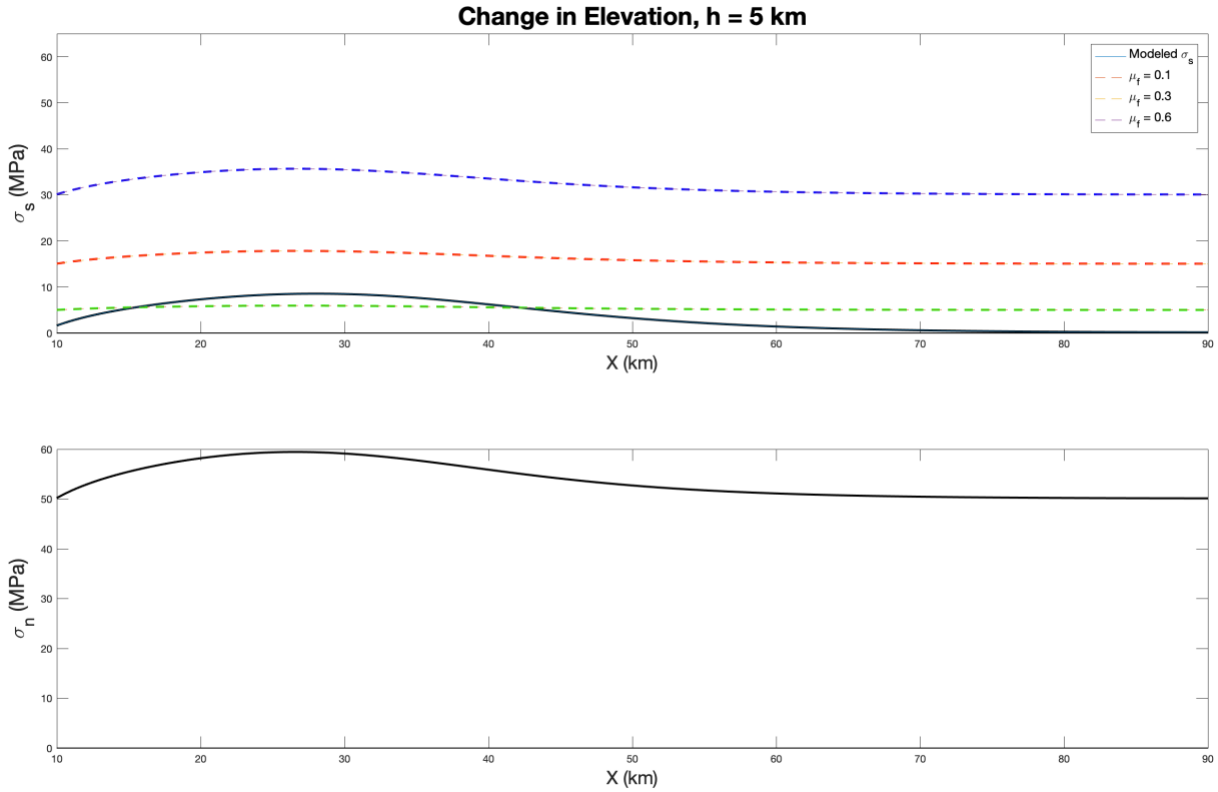

Figure 17: Normal and Shear tractions on detachment surface with a change in elevation of 5 km.

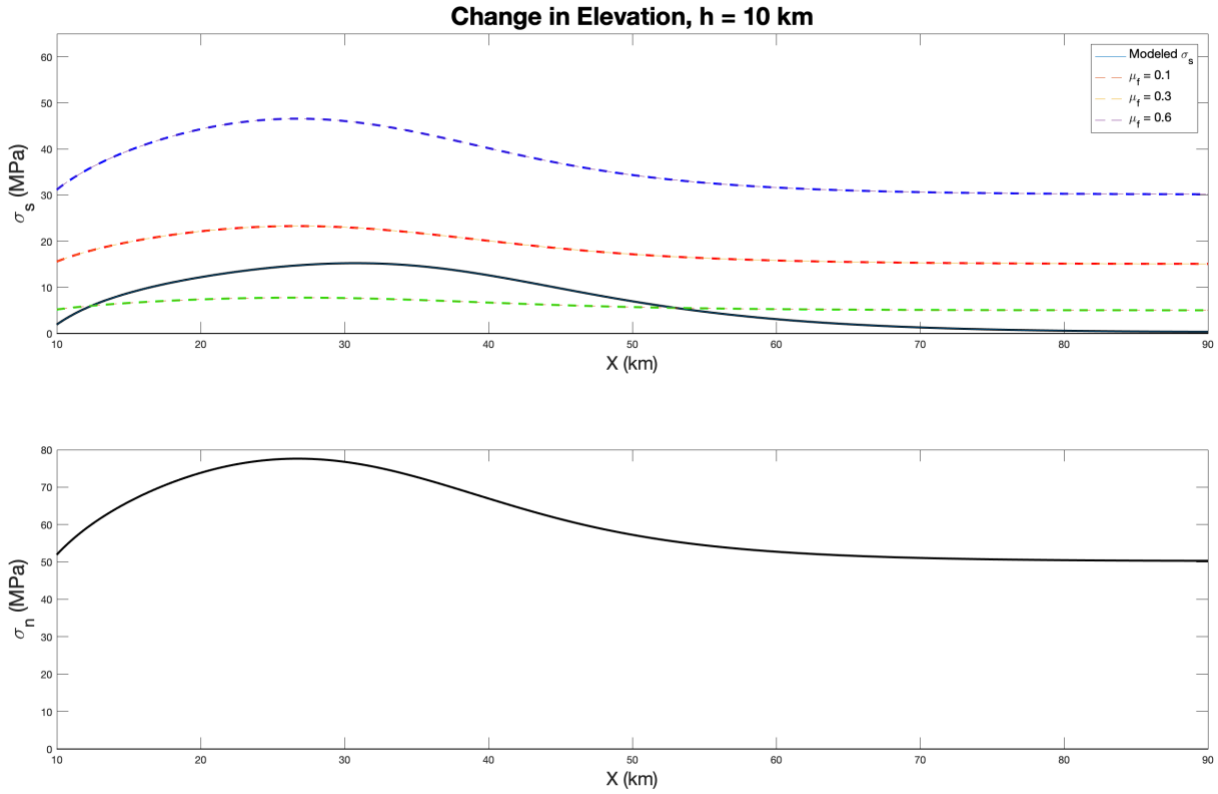

Figure 18: Normal and Shear tractions on detachment surface with a change in elevation of 10 km.

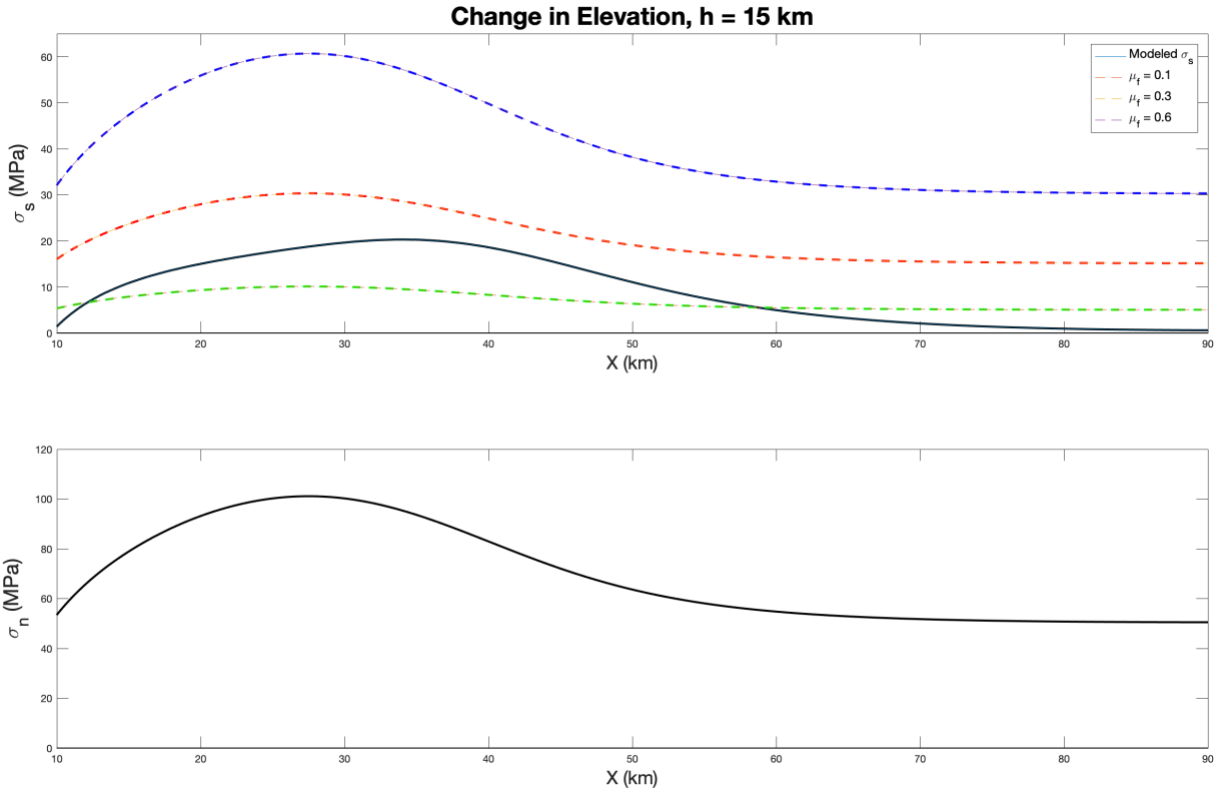

Figure 19: Normal and Shear tractions on detachment surface with a change in elevation of 15 km.

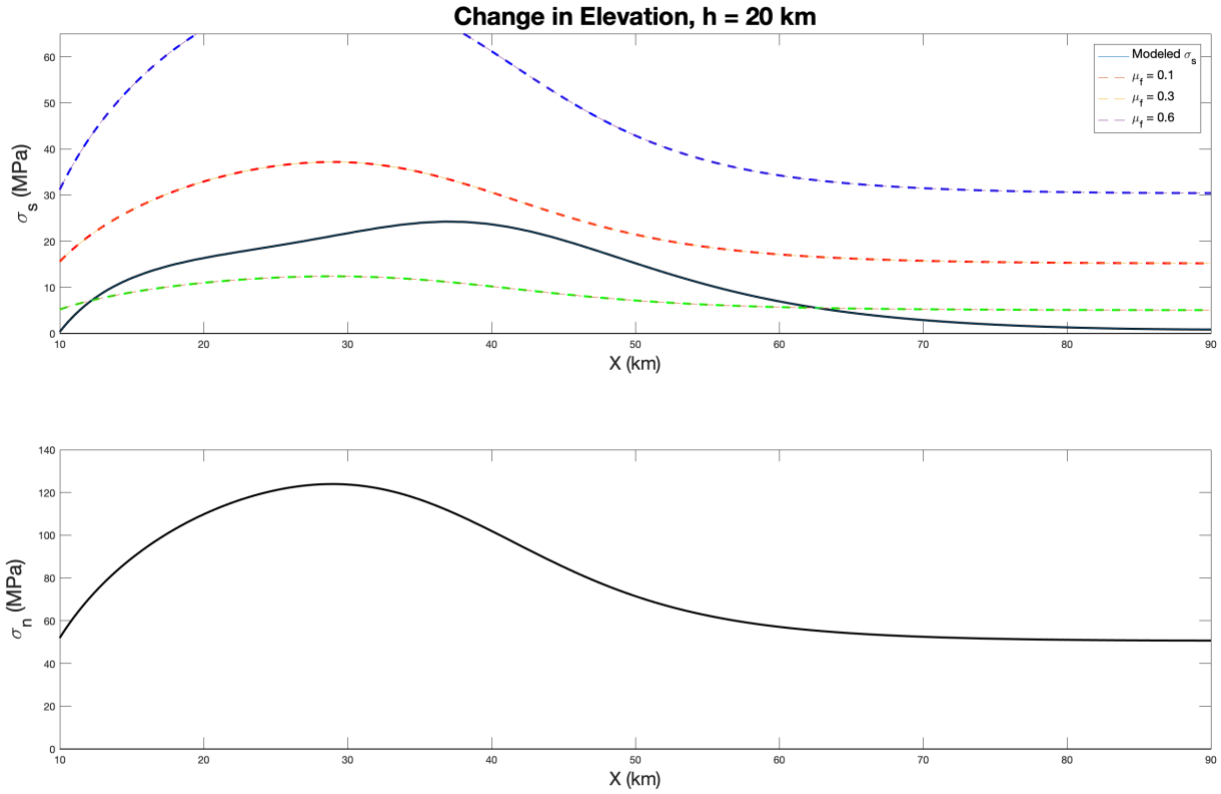

Figure 20: Normal and Shear tractions on detachment surface with a change in elevation of 20 km.

Simulations are also run with varying slope constant, *k,* and a constant topographic relief, *h*, defined within the logistic function, Equation (1). Results are shown for two simulations, both for an extensional far field stress regime with 10 kilometers of topographic relief. The slope is varied by a factor of 2 and resulting shear stresses along with critical shear stress criterion are shown for both simulations (Figure 21).

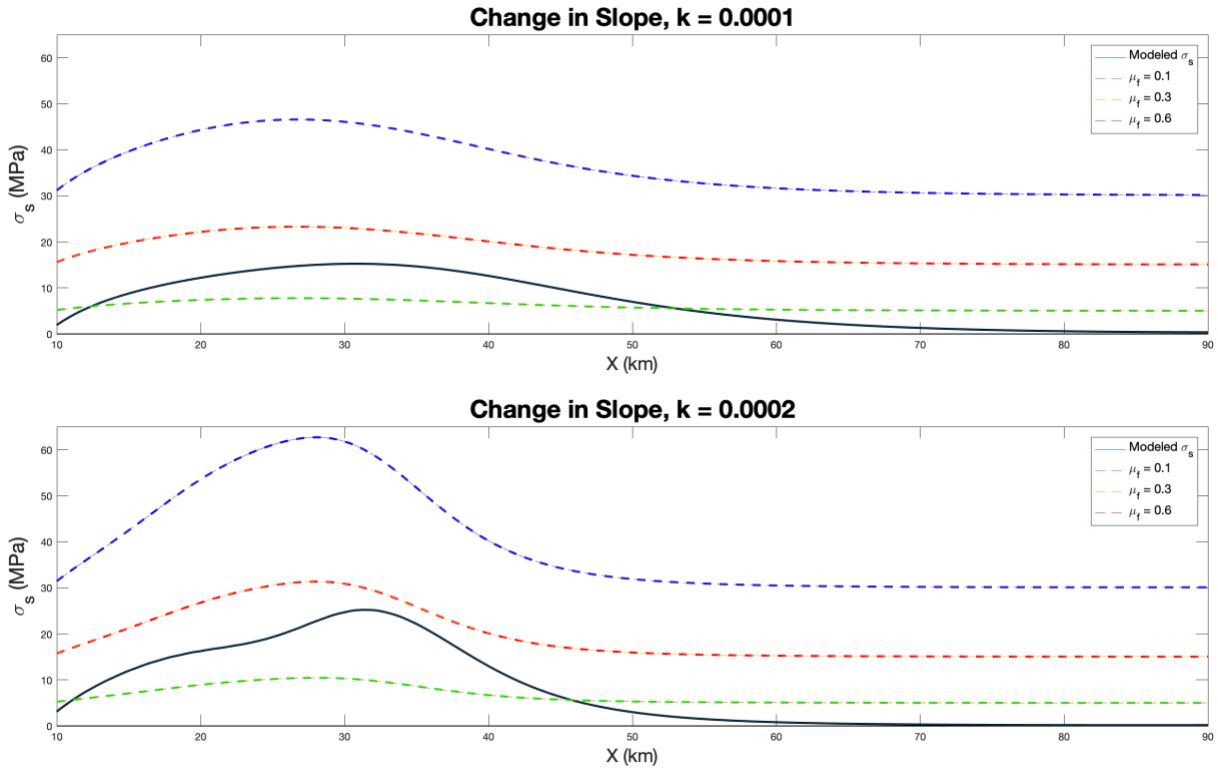

Figure 21: Calculated shear stress and critical shear stresses plotted for an extensional far field stress regime with 10 kilometers of topographic relief. The slope constant, k, is varied from 0.0001 (top) to 0.0002 (bottom) to show how the resulting shear stresses vary.

Phi

Another measure of slope stability, ϕ, is plotted for an extensional far field stress regime and a total change in elevation of 10 kilometers (Figure 22). The model domain is clipped to focus in on the near subsurface, within 5 km depth, which is the area relevant to failure and approximate location of the Brian Head Formation. A contour plot is shown between 0 and 1, values of ϕ closer to 1 indicate areas of slope instability while values close to 0 indicate stability. ϕ values approach one closer to the surface along the slope of topography, agreeing with previous stability analysis. Specifically, there is a concave upward alignment of contour lines at approximately $x = 30\ km$, agreeing with the peaks in shear stresses occurring farther south than the inflection point.

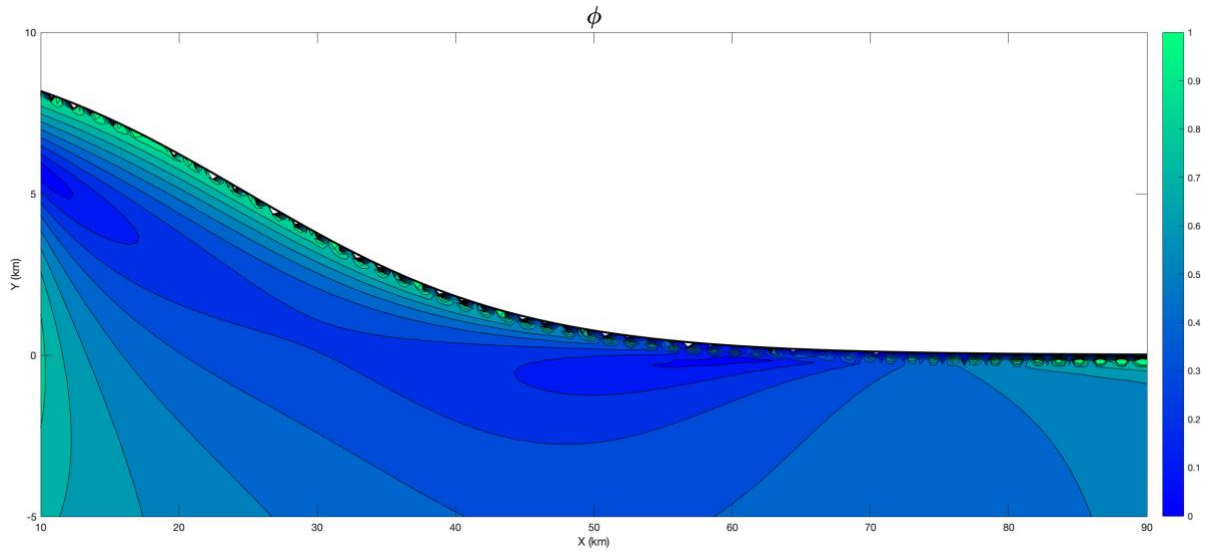

Figure 22: Distribution of ϕ below the topographic surface. Topography is defined with a change in elevation of 10 km, and far field stresses are extensional.

DISCUSSION

In the absence of additional triggering mechanisms, the results analyze the role of topographically driven stress perturbations in the subsurface stress distribution, and subsequently on the shear stresses along a potential detachment surface. I provide evidence for constraints on the regional far field stresses at the time of the slide. I show that with increasing topographic relief, shear stresses are increased along the potential detachment surface. And I show that with only small topographic relief, and hypothetical inclusion of triggering events, it is possible to model landslide initiation of the massive SGS.

More broadly, the results indicate that I have built a functioning model that can serve as the basis of a more complex version moving forward. As was discussed, a primary goal of this project was to create the framework of a model for the SGS that can be further manipulated to include more complex processes to trigger initiation. In the Future Work section, I will discuss the ways in which research on the SGS project will inform the model built thus far in this project and add elements to capture the full range of potential initiation factors.

Implications of Detachment Surface Stresses

Gravity driven landslides initiate when a detachment surface fails under shear stress. Using the results, I analyze zones of shear failure along the idealized Brian Head Formation under varying topographic and far field stress conditions. When the calculated shear stresses along the detachment surface exceed critical shear stresses, I conclude that failure is probable, dependent upon the mechanical properties of the rocks.

In the model, shear stress is analyzed as it relates to two parameters, the topography and the far field stresses. Topography includes two elements that control shear stresses, the absolute change in elevation and the slope.

Variance in far field stresses indicates slight influence on initiation conditions. The influence of far field stresses lies in the differential stresses they allow in the subsurface. While compressional or thrust faulting stress regimes allow for high differential stresses, it is unlikely that they influenced slide initiation due to known tectonic processes at the time (i.e., magmatic intrusions). Between extensional and lithostatic regimes, lithostatic stress allows less differential stress beneath the topography, and therefore is less preferential to initiate sliding. That being said, it is clear that topography has far greater influence on slide initiation than the background stress state.

Shear stresses along the Brian Head Formation are directly influenced by the slope of the topography. Equations (7a) and (7b) show the dependency of the normal and shear stresses with an angle, θ, calculated from the topographic surface. It is important to note that based on Equation (1), the topographic surface has very shallow slopes which reach a maximum as $x = 25{,}000$ (the inflection point) and trends toward 0 as x increases. These observations are shown in the calculated normal and shear stresses in Figures 17-20. Both stress values have an apparent horizontal

asymptote with perturbations centered and maximum at as $x = 25{,}000$ while approaching the horizontal asymptote as x increases.

Again, looking at Equations (7a) and (7b), and thinking about the perturbances in σ_s and σ_n values occurring where there is a non-zero topographic slope, one can see that it is the sine terms in those equations that control the perturbations in these stress values. One important observation is that as θ deviates from 0 and the sine terms become nonzero, $\sin(2\theta)$ deviates from zero faster than $\sin(\theta)$ does. This observation results in a greater perturbation from the asymptotic value in σ_s than in σ_n, and allows σ_n to climb above critical shear stress values, $\sigma_s{}^*$, when theta deviates from 0. Thus, paleo-conditions that have higher slopes in the foothills of Marysvale favor slide initiation.

Further failure criteria, not considered in this thesis, could include analysis of the angle of the detachment surface from the horizontal. Considering this simpler model shown in Figure 23, failure criteria can be calculated based on the angle β. When the tangent of β, in radians, exceeds the frictional strength of the material, we can estimate failure (Turcotte and Schubert, 2014). Considering this failure criteria alongside that of the calculated shear stresses could provide deeper insight into the driving factors of initiation, namely if the slope is more influential than the magnitude of subsurface stresses. If it is possible to induce the massive SGS emplacement event only using analysis of the slope of the Brian Head Formation, it is likely that the slope of the detachment surface is the controlling factor of initiation. If instead simple analysis of the slope fails to create a significant detachment zone, it is more likely that the stresses play a more direct role, and far field as well as topographic perturbances are the controlling parameters.

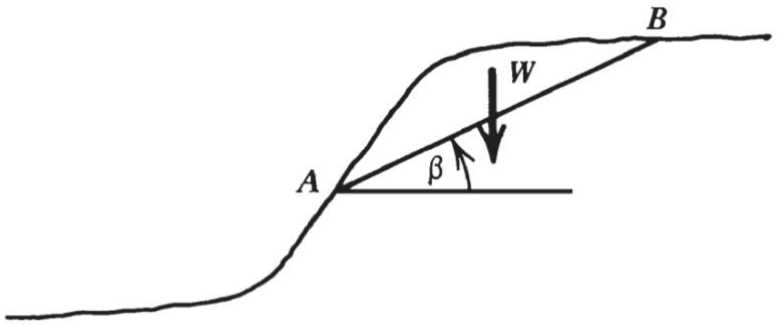

Figure 23: A rock slope with potential detachment surface AB, defined by the angle β. W refers to the weight of the rock mass above the detachment surface.

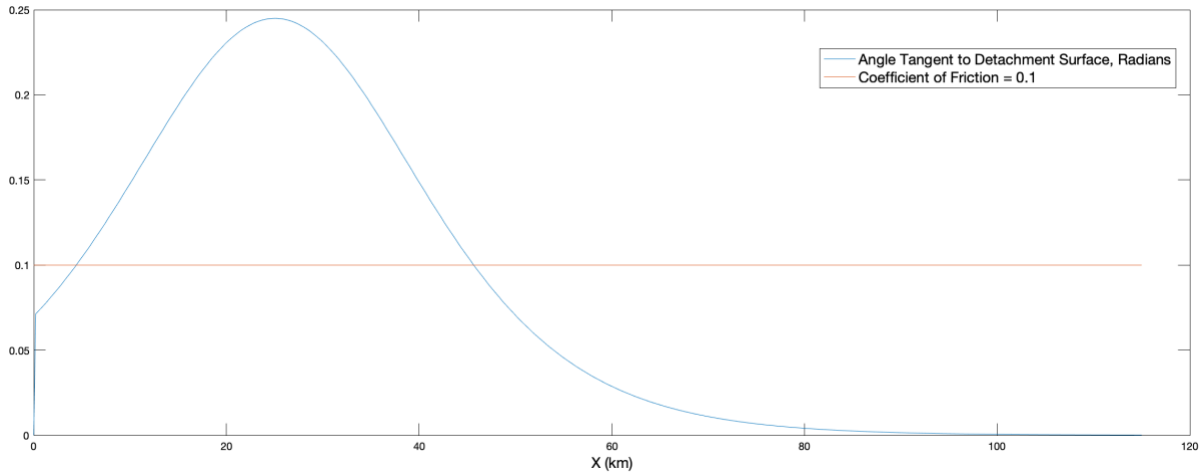

Figure 24: Simple failure criteria considering tangent angle, in radians, of detachment surface vs. coefficient of friction.

This parallel failure analysis underscores the importance of continued refinement of the understanding of the detachment surface. Not only are the mechanical properties of the Brian Head of interest, which will be discussed shortly, but also the geometry of the Brian Head before sliding initiated. The slope of the detachment surface is highly idealized in this model to be parallel to topography, and the results indicate that the slope of this surface is critically important. Further, if the slope of the Brian Head changed over time, from sub-horizontal to gently dipping, this could be a potential triggering event.

Limitations

In the extensional simulations shown in Figures 17-20, calculated shear stresses commonly exceed the failure criterion for $\mu_f = 0.1$, but do not exceed for $\mu_f = 0.3, 0.6$. While changes in elevation of 15 or 20 km may be overly drastic in terms of a realistic paleo-topography, even a change of elevation of 10 km indicate a zone of approximately 50 km for which shear stresses exceed failure criterion. These results showing massive lengths over which failure is possible in part explains the enormous size of the SGS and how it was possible for this massive volume to be catastrophically emplaced in a single detachment event.

Even though large areas of potential failure can be produced in the model, it is important to note that this failure is for $\mu_f = 0.1$, which is a relatively low frictional strength. While the frictional strength of the Brian Head formation is yet unknown, and we know it is weaker than surrounding rock layers, it is unclear whether the true frictional strength of the Brian Head is close to 0.1. If I consider a potentially larger frictional strength without overly drastic topography, i.e., no more than 10 km change, the results indicate that there may be just a very small area of instability.

But these results are to be expected. Potential trigger events of the SGS have been referenced here and explicitly not included in the model. Results of this model indicate a state of stress solely defined by the topography and far field stresses. Inclusion of the triggering events previously discussed will

take the shear stresses calculated here as a starting point to be further influenced by those triggers. Thus, a small area of instability in the current model could be indicative of a very large area of instability when trigger events are included.

If we consider potential drivers of increased shear stress along with fluidization of the Brian Head formation, increasing pore pressure and decreasing the frictional strength, a small detachment zone indicated in my results can grow much larger.

Triggering Mechanisms

Trigger events come in two forms: drivers of increased shear stresses along the Brian Head or drivers of decreased frictional strength of the Brian Head. Hypotheses for initiation triggers for the SGS include lateral spreading along the Ruby's Inn thrust fault, magmatic intrusions, and elevated pore fluid pressures.

Volcanic activity in Marysvale continued to influence the stress distributions in the area beyond simply controlling the pre-existing topography. Biek et al. 2019 suggest that inflation of the volcanic pile from either a batholith underlying the heart of the volcanic field, or laccolith intrusions above the batholith could have quickly increased the topographic extent of the Monroe Peak Caldera, driving up shear stresses along the Brian Head, and also tilted the strata beneath the volcanic pile. Smaller scale sector collapse has been documented as a result of laccolith intrusion (Hacker et al., 2002), suggesting that larger scale failures could be generated by magmatic intrusions as well.

Biek et al. (2019) concur with previous literature on the Marysvale area (Davis and Rowley, 1993; Merle et al., 1993) suggesting that the Paunsaugunt thrust system formed in part due to emplacement of batholithic intrusions into the volcanic field. Hacker et al. (2014), as well suggest that laccolith intrusion could have driven lateral spreading along the Paunsaugunt thrust system, triggering the Markagunt Gravity Slide.

Lateral spreading is known to increase local stress perturbations and initiate landslides (van Wyk de Vries and Francis, 1997). In the case of the SGS, lateral spreading occurs in the basement rocks beneath the volcanic pile due to thrusting to the south of the Ruby's Inn Thrust Fault (Figure 4). The basement rocks thrusting southward along the fault results in local extension in the area to the north, further exaggerating the topographic relief, and driving stress perturbations within the ridge.

The Marysvale Volcanic Field is known to be active before and around the time of the slide, and the same is true of the Ruby's Inn thrust fault. From the literature, it is clear that these processes have a direct influence on landslide initiation. Therefore, both of these factors, magmatic intrusion and lateral spreading, should be considered as present and influential in modeling the initiation of the SGS.

Finally, another element of complexity to be added to the model is pore fluid pressure. Continuing work on the SGS indicates that elevated pore fluid pressure may have been a very serious influence on slide mobility and were thus present in pre-slide conditions (Braunagel et al., 2020). Increase in

the pore fluid pressure in the Brian Head Formation would drive down the frictional strength of the unit, potentially initiating failure.

Fluid pressure can be taken into account in the model in two ways. First, pore fluid pressure would have an impact on the far field state of stress as defined in the model. Secondly, failure criterion against which we analyze calculated shear stresses can be influenced by fluid pressure. Increased pore fluid pressure lowers failure criteria, regardless of the true frictional strength of the Brian Head Formation, as shown in Figure 25. Significant fluid pressures, between hydrostatic and lithostatic, are possible given the volcanic field and hydrothermal fluids that may have spread therefrom (e.g., Pearce et al., 2020).

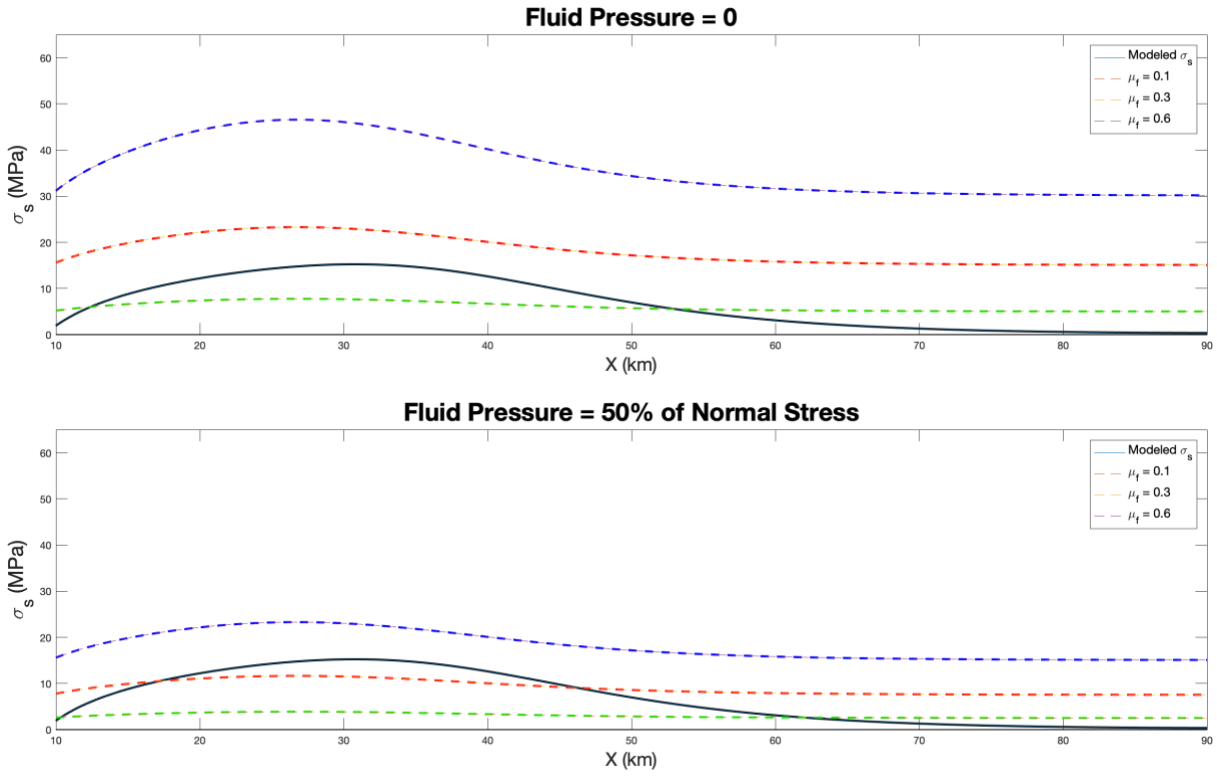

Figure 25: Calculated shear stress and critical shear stresses plotted for an extensional far field stress regime with 10 kilometers of topographic relief. Pore fluid pressure is varied from 0 to 50% of the normal stress to show how increases in fluid pressure can decrease the frictional strength of the material and increase the potential zone of detachment.

The model developed in this thesis has been validated to accurately complete the first step in modeling the initiation of the SGS and creates ample opportunity to add complexity in a way that fully captures the pre-slide conditions of the SGS.

CONCLUSIONS

Initiation of the Sevier Gravity Slide is highly complex and can provide insights into the mechanics of the slide and other analogous terrestrial long runout landslides and is worth investigating. Creation of an ideal model that factors in these various complexities is difficult, but worthwhile given the insights to gain. The model developed in this project serves as a first step in creating the ideal model. The methods used and developed here serve as a framework for future work, added factors of complexity will be built into the existing scripts which serve as the computational backbone of the model.

I modeled the paleo-environment of the SGS investigating the influence of topography and far field stresses on the subsurface stress distributions, focused on results that provide insight into the paleo-conditions necessary for failure and landslide initiation. I calculate subsurface stress distributions using BEM and further derive stability criteria for analyzing potential initiation. I conclude the following:

1. I have created a model that can simulate paleo-conditions of the SGS within a framework that is verified against an analytical solution provided by Savage et al. (1985). Results verified include complete stress distributions beneath topography, and thus normal and shear stresses calculated at any point.

2. Increased topographic relief in the paleo-environment, modeled by varying the total change in elevation in a logistic function, drives increased stress perturbations within the ridge, thus favors initiation of a landslide.

3. Lithostatic and extensional stress regimes favor slide initiation over compressive regimes. Moreover, extensional regimes are preferable over lithostatic as differential stresses, and thus shear stresses, are higher in magnitude, favoring failure.

4. The most unstable region is roughly beneath the area of highest slope in topography, the inflection point in the logistic function. While hypothesized that the maximum area of instability would be directly under the inflection point (25,000 m), I find that with increasing topographic relief, the maximum shear stresses, and thus areas of instability, creep southward from 25,000 m. With a change in elevation of 20 km, the maximum shear stress is at approximately 40,000 m, near the bottom of the slope.

5. I find that the areas of instability inferred from the normal and shear stresses along a hypothesized Brian Head Formation can be verified using the stability measurement Phi, developed by Reid and Iverson (1992).

6. While the model is currently able to simulate and constrain paleo-conditions of the SGS, it is understood that initiation of the slide was influenced by more than the static state of stress

due to topography and far field stresses (Hacker et al., 2014; Biek et al., 2019). Thus, triggering events must be incorporated into the model in the future.

7. Finally, the model built thus far was crafted with the intention of adding more elements, such as the Ruby's Inn thrust fault, to represent events that may trigger initiation. The model is well prepared to incorporate future work done on these trigger events seamlessly.

RECOMMENDATIONS FOR FUTURE WORK

Future work will be necessary to complete an accurate model of pre-slide conditions of the SGS and properly investigate initiation. Work is needed in two categories, refinement of constants used in the model from mapping and experimental data, and addition of triggering events into the model.

There is much to be done constraining the parameters and constants used throughout the model. This refinement will be the result of experiments done on rock specimens collected from the region as well as further collection and interpretation of mapping data for the SGS. Accurate modeling of SGS will need further refinement of:

1. Geometry and relief of topographic surface.
2. Location of the ramp fault.
3. Location and geometry of the detachment surface and the Brian Head Formation
4. Mechanical properties of rocks in the areas, specifically Mt. Dutton Formation and Brian Head Formation

More than just refinement of certain inputs within the model, additional components must be incorporated into the model to capture the influences of SGS initiation. In many ways, the work done in this thesis project can be viewed as priming for future work to be done. What is presented here acts as a built framework and starting point for the complete model.

Within the simulations presented here, only one surface is considered within the model, the topographic surface. For this surface we define specific boundary conditions, specifically that it is a free surface that maintains zero normal and shear stress. I use this surface in Equations (5) and (6) to solve for the subsurface stress distribution, as influenced by topography. The model is built such that a second surface can be added along with a second set of boundary conditions, which can influence the subsurface stress distribution calculated.

For example, the Ruby's Inn thrust fault could be added as a second surface, with boundary conditions inferred by proposed activity along the fault and include influence from fault activity in the subsurface stress distribution. It is important to remember that in BEM, displacements are calculated along the given surface as a middle step towards calculating stresses around the surface. With topography, these calculated displacements were meaningless because we treated the body above topography to be nothing, but with a thrust fault beneath the surface, we can calculate the slip along the fault due to the overlying topography, and then calculate the resulting stress perturbances due to that slip in an iterative process. Stress perturbations induce slip, slip induces stress perturbations, and eventually we induce catastrophic failure and initiation of the SGS.

Another additional influence will be magmatic growth and intrusions around the Monroe Peak Caldera region. This can be modeled in many ways. For one, it can be modeled as a static increase in height of the volcanic pile. More informative would be modeling growth of a magmatic intrusion over time in an iterative process, to calculate the influence in stress perturbations from growth.

These processes can be combined. As discussed, magmatic growth in Marysvale is hypothesized to have induced lateral spread along the Ruby's Inn thrust fault. In the future, it will be important to

incorporate both of these mechanisms into the model to test this hypothesis. Within the framework of my results, these mechanisms will work to increase the stress perturbances caused by topography and initiate detachment. With future work, the model used in this project can be developed into a model that sufficiently idealized the initiation process of the SGS.

REFERENCES CITED

Anders, M.H., Aharonov, E., and Walsh, J.J., 2000, Stratified granular media beneath large slide blocks: Implications for mode of emplacement: Geology, v. 28, p. 971–974, doi:10.1130/0091-7613(2000)28<971:SGMBLS>2.0.CO;2.

Anderson, J.J., and Rowley, P.D., 1975, Cenozoic Geology of Southwestern High Plateaus of Utah: Geological Society of America, 127 p.

Biek, R.F., Rowley, P.D., Anderson, J.J., Maldonado, F., Moore, D.W., Hacker, D.B., Eaton, J.G., Hereford, R., Filkorn, H.F., and Matyjasik, B., 2015, Geologic map of the Panguitch 30' x 60' quadrangle, Garfield, Iron and Kane Counties, Utah: Utah Geological Survey, doi:10.34191/M-270dm.

Biek, R.F., Rowley, P.D., Hacker, D.B., 2019, The Gigantic Markagunt and Sevier Gravity Slides Resulting from Mid-Cenozoic Catastrophic Mega-Scale Failure of the Marysvale Volcanic Field, Utah, USA, 2019, in The Gigantic Markagunt and Sevier Gravity Slides Resulting from Mid-Cenozoic Catastrophic Mega-Scale Failure of the Marysvale Volcanic Field, Utah, USA, Geological Society of America, p. 1–108, doi:10.1130/2019.0056(01).

Braunagel, M.J., Griffith, W.A., Biek, R.F., Hacker, D.B., 2020, Evidence for Catastrophic Emplacement of the Marysvale Gravity Slide Complex Aided by Thermal Pressurization of Shear Zone Fluids, Geological Society of America Abstracts with Programs, Vol 52, No. 6, Abstracts, doi: 10.1130/abs/2020AM-352070.

Crouch, S.L., Starfield, A.M., and Rizzo, F.J., 1983, Boundary Element Methods in Solid Mechanics: Journal of Applied Mechanics, v. 50, p. 704–705, doi:10.1115/1.3167130.

Davis, G.H., and Rowley, P.D., 1993, Miocene thrusting, gravity sliding, and near-surface batholithic emplacement, Marysvale volcanic field, southwestern Utah: Eos, Transactions, American Geophysical Union, v. 74, p. 647.

Fleming, R.W. and A. M. Johnson, 1989, Structures associated with strike-slip faults that bound landslide elements, Engineering Geology, 27, p. 39-114).

Goren, L., and Aharonov, E., 2007, Long runout landslides: The role of frictional heating and hydraulic diffusivity: Geophysical Research Letters, v. 34, p. L07301, doi:10.1029/2006GL028895.

Griffith, W.A., Becker, J., Cione, K., Miller, T., and Pan, E., 2014, 3D topographic stress perturbations and implications for ground control in underground coal mines: International Journal of Rock Mechanics and Mining Sciences, v. 70, p. 59–68, doi:10.1016/j.ijrmms.2014.03.013.

Hacker, D.B., Biek, R.F., and Rowley, P.D., 2014, Catastrophic emplacement of the gigantic Markagunt gravity slide, southwest Utah (USA): Implications for hazards associated with sector collapse of volcanic fields: Geology, v. 42, p. 943–946, doi:10.1130/G35896.1.

Hacker, D.B., Holm, D.K., Rowley, P.D., and Blank, H.R., 2002, Associated Miocene laccoliths, gravity slides, and volcanic rocks, Pine Valley Mountains and Iron Axis region, southwestern Utah, in Lund, W.R., ed., Field Guide to Geologic Excursions in Southwestern Utah and Adjacent Areas of Arizona and Nevada: U.S. Geological Survey Open-File Report 02-0172, p. 235–283.

Highland, L., 2004, Landslide Types and Processes, Fact Sheet 2004-3072:, https://pubs.usgs.gov/fs/2004/3072/pdf/fs2004-3072.pdf.

Hubbert, M.K., and Rubey, W.W., 1959, Role of Fluid Pressure in Mechanics of Overthrusting Faulting, Geological Society of America Bulletin, v. 70, p. 115, doi:10.1130/0016-7606(1959)70[115:ROFPIM]2.0.CO;2.

Hürlimann, M., Garcia-Piera, J.O., and Ledesma, A., 2000, Causes and mobility of large volcanic landslides: application to Tenerife, Canary Islands: Journal of Volcanology and Geothermal Research, v. 103, p. 121–134, doi:10.1016/S0377-0273(00)00219-5.

Jaeger, J.C., Cook, N.G.W., and Zimmerman, R.W., 2007, Fundamentals of rock mechanics: Malden, MA, Blackwell Pub, 475 p.

Legros, F., 2002, The mobility of long-runout landslides: Engineering Geology, v. 63, p. 301–331, doi:10.1016/S0013-7952(01)00090-4.

Martel, S.J., 2004, Mechanics of landslide initiation as a shear fracture phenomenon: Marine Geology, v. 203, p. 319–339, doi:10.1016/S0025-3227(03)00313-X.

Martel, S.J., and Muller, J.R., 2000, A Two-dimensional Boundary Element Method for Calculating Elastic Gravitational Stresses in Slopes: Pure and Applied Geophysics, v. 157, p. 989–1007, doi:10.1007/s000240050014.

Merle, O.R., Davis, G.H., Nickelsen, R.P., and Gourlay, P.A., 1993, Relation of thin-skinned thrusting of Colorado Plateau strata in southwestern Utah to Cenozoic magmatism: Geological Society of America Bulletin, v. 105, p. 387– 398, doi:10.1130/0016-7606(1993)105<0387: ROTSTO >2.3.CO;2.

Pearce, R. K., Sánchez de la Muela, A., Moorkamp, M., Hammond, J. O. S., Mitchell, T. M., Cembrano, J., et al. (2020). Reactivation of fault systems by compartmentalized hydrothermal fluids in the Southern Andes revealed by magnetotelluric and seismic data. Tectonics, 39, e2019TC005997. https://doi.org/10.1029/2019TC005997

Reid, M.E., and Iverson, R.M., 1992, Gravity-driven groundwater flow and slope failure potential: 2. Effects of slope morphology, material properties, and hydraulic heterogeneity: Water Resources Research, v. 28, p. 939–950, doi:10.1029/91WR02695.

Rowley, P.D., Cunningham, C.G., and Kaplan, A.M. Geologic Map of the Monroe SE Quadrangle, Sevier and Piute Counties, Utah: Utah Geological Survey.

Rowley, P.D., Vice, G.S., McDonald, R.E., Anderson, J.J., Machette, M.N., Maxwell, D.J., Ekren, E.B., Cunningham, C.G., Steven, T.A., and Wardlaw, B.A., 2005, Interim geologic map of the

Beaver 30' x 60' quadrangle, Beaver, Piute, Iron, and Garfield Counties, Utah: Utah Geological Survey.

Varnes, D.J., 1978, Slope movement types and processes, in Schuster, R.L., and Krizek, R.J., eds., Landslides—Analy- sis and control: National Research Council, Washington, D.C., Transportation Research Board, Special Report 176, p. 11–33.

Savage, W.Z., Swolfs, H.S., and Powers, P.S., 1985, Gravitational Stresses in Long Symmetric Ridges and Valleys: International Journal of Rock Mechanics and Mining Sciences, v. 22, p. 291–302.

Steven, T.A., Rowley, P.D., and Cunningham, C.G., 1984, Calderas of the Marysvale Volcanic Field, west central Utah: Journal of Geophysical Research, v. 89, p. 8751, doi:10.1029/JB089iB10p08751.

Turcotte, D.L., and Schubert, G., 2014, Geodynamics: Cambridge, United Kingdom, Cambridge University Press, 623

Weidinger, J.T., Korup, O., Munack, H., Altenberger, U., Dunning, S.A., Tippelt, G., and Lottermoser, W., 2014, Giant rockslides from the inside: Earth and Planetary Science Letters, v. 389, p. 62–73, doi:10.1016/j.epsl.2013.12.017.

van Wyk de Vries, B., and Matela, R., 1998, Styles of volcano-induced deformation: numerical models of substratum flexure, spreading and extrusion: Journal of Volcanology and Geothermal Research, v. 81, p. 1–18, doi:10.1016/S0377-0273(97)00076-0.